Helicity Asymmetries in Double-Charged-Pion Photoproduction from Hydrogen with Circularly Polarized Photons

Steffen Strauch

The George Washington University

May 27, 2004

Abstract

Helicity asymmetries in double-charged-pion photoproduction from unpolarized hydrogen with circularly polarized photons have been studied for the first time in the resonance region. The data were taken as part of the CLAS g1c run group with incident photons in the energy range between 0.5 GeV and 2.3 GeV. Owing to the large angular acceptance of the CLAS detector, complete angular distributions of the helicity asymmetries were measured. The large cross-section asymmetries exhibit strong sensitivity to the kinematics of the reaction and provide valuable information on the reaction dynamics. This document summarizes the analysis of the data.

Contents

1 Introduction

Many nucleon resonances in the mass region above 1.6 GeV decay predominantly through $\Delta\pi$ or $N\rho$ intermediate states into $N\pi\pi$ final states (see the Particle-Data-Group review, [1]). This makes electromagnetic exclusive double-pion production an important tool in the investigation of N^* structure and reaction dynamics, as well as in the search for "missing" baryon states. Unpolarized cross-section measurements of double-pion electroproduction have recently been reported in [2]. Further constraints are to be found in polarization observables.

Here, we discuss the analysis of a measurement of the $\gamma p \to p\pi^+\pi^-$ reaction, where the photon beam is circularly polarized (with helicity $\lambda_\gamma = \pm 1$) and no nuclear polarizations (target or recoil) are specified. The general form of the cross section can then be written as

$$\sigma^\pm = \Sigma \pm P_\gamma \Delta \,, \tag{1}$$

where Σ and Δ are the unpolarized and polarized cross sections. The degree of circular polarization is P_γ. The cross-section asymmetry, obtained by flipping the beam polarization, is given by:

$$A = \frac{1}{P_\gamma} \cdot \frac{\sigma^+ - \sigma^-}{\sigma^+ + \sigma^-} = \frac{\Delta}{\Sigma} \,. \tag{2}$$

For this kind of study, a three-body final state is required, since reactions with only two-body final states are always coplanar and have identical cross sections for unpolarized or circularly polarized photons [3], so that $\Delta = 0$. The asymmetry A vanishes in full coplanar kinematics.

2 Reaction

The $\gamma p \to p\pi^+\pi^-$ reaction with its three-body final state is described by a five-fold-differential cross section. Figure 1 illustrates the kinematics of the reaction, where $\vec{k}$ and $\vec{p}$ are the center-of-mass photon and target momenta, and $\vec{a}$, $\vec{b}_1$, and $\vec{b}_2$ are the momenta of the final-state particles in their three different configurations: $a[b_1, b_2] = p[\pi^+, \pi^-]$, $\pi^+[\pi^-, p]$, or $\pi^-[p, \pi^+]$. Following the convention of Schilling, Seyboth, and Wolf [4], the normal vector $\vec{y}$ to the production plane is given by $\hat{y} = \hat{k} \times \hat{q}$ where $\hat{q}$ points into the direction of $\vec{b}_1 + \vec{b}_2$. The polar angle of $\hat{q}$ is given by

$$\cos\theta_{\mathrm{cm}} = \hat{k} \cdot \hat{q} \,. \tag{3}$$

The polar and azimuthal angles of b_1 (decay angles) are given in the rest frame of the $b_1 b_2$ system. The commonly used helicity, Gottfried-Jackson, or Adair coordinate systems differ by the choice of the z axis; see Table 1.

$$\cos\theta = \hat{b}_1 \cdot \hat{z} \,, \qquad \cos\phi = \frac{\hat{y} \cdot (\hat{z} \times \hat{b}_1)}{|\hat{z} \times \hat{b}_1|} \,, \quad \text{and} \quad \sin\phi = -\frac{\hat{x} \cdot (\hat{z} \times \hat{b}_1)}{|\hat{z} \times \hat{b}_1|} \,. \tag{4}$$
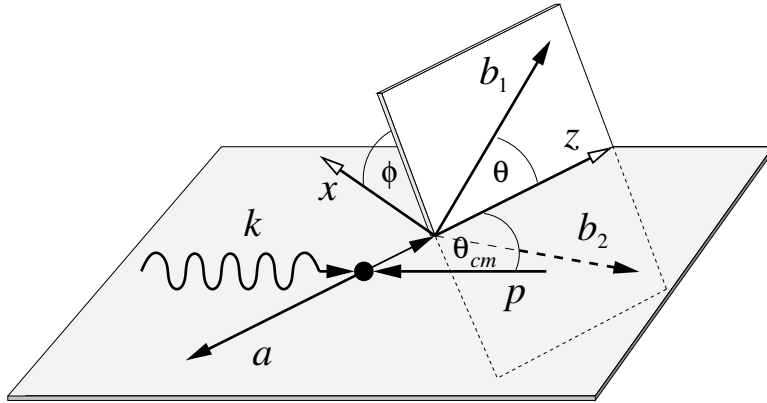
Figure 1: Definitions of variables for the $\gamma p \to ab_1 b_2$ reaction in the helicity system. Indicated are the four-momentum vectors of the participating particles. θ_{cm} is defined in the center-of-mass frame of the γp system, and θ is defined in the rest frame of the $b_1 b_2$ system.

Table 1: Coordinate systems

System	z axis
Helicity	Direction of $\vec{b}_1 + \vec{b}_2$ in the overall c.m. system
Gottfried-Jackson	Direction of flight of the incoming photon in the $b_1 b_2$ rest frame
Adair	Direction of flight of the incoming photon in the c.m. system

The quasi-two-particle mechanisms involving the production and subsequent decay of Δ and ρ resonances in the intermediate state ($\Delta^{++}\pi^-$, $\Delta^0\pi^+$, and $p\rho$) make the main contributions to the $\gamma p \to p\pi^+\pi^-$ reaction. Thews [5] has studied decay angular distributions for the general case of a two-body inelastic reaction $\gamma + N \to V + N^*$, where the photon is linearly or circularly polarized, the nucleon is unpolarized and V and N^* are mesons and baryons with arbitrary spins. K. Schilling, P. Seyboth, and G. Wolf discussed the more specific case of photoproduction of vector mesons by polarized photons on an unpolarized nucleon and their subsequent decay distribution [4]. The decay angular distributions are functions of the density matrix elements ρ_{ij} and are given by

$$W^\pm(\cos\theta, \phi) = W^0(\cos\theta, \phi) \pm P_\gamma W^3(\cos\theta, \phi) \tag{5}$$

4

with

$$W^0(\cos\theta,\phi) = \frac{3}{4\pi}\left(\frac{1}{2}(1-\rho_{00}^0)+\frac{1}{2}(3\rho_{00}^0-1)\cos^2\theta\right.$$
$$\left.-\sqrt{2}\Re\rho_{10}^0\sin 2\theta\cos\phi-\rho_{1-1}^0\sin^2\theta\cos 2\phi\right), \qquad (6)$$

$$W^3(\cos\theta,\phi) = \frac{3}{4\pi}\left(+\sqrt{2}\Im\rho_{10}^3\sin 2\theta\sin\phi+\Im\rho_{1-1}^3\sin^2\theta\sin 2\phi\right). \quad (7)$$

Since ρ^3 is made of imaginary parts of products of helicity amplitudes, a nonzero value for W^3 implies interference terms between amplitudes with different phases. A detailed study of the decay angular distribution of the Δ^{++}, Δ^0, or ρ can only be performed after isolating these channels. This is not the scope of the first stage of this analysis.

3   Experiment

The $\gamma p \to p\pi^+\pi^-$ data were obtained with the CEBAF-Large-Acceptance Spectrometer (CLAS) [6] at Jefferson Lab. Longitudinally polarized electrons with an energy of 2.445 GeV were incident on the thin radiator of the Hall-B Photon Tagger [7] and produced circularly polarized tagged photons in the energy range between 0.5 GeV and 2.3 GeV. The collimated photon beam irradiated a liquid-hydrogen target. The degree of circular polarization of the photon beam can be determined from the electron-beam polarization and the ratio of photon and incident electron energy; see Sec. 4.2.1. Characteristics of the experiment are summarized in Table 2. More information can be found in [8] and on the g1c data set, calibration, and cooking WEB page [9].

To identify the reaction channel, the missing-mass technique was used, requiring the detection of at least two out of three charged final-state particles (p, π^+, and π^-) in CLAS, see Sec. 4.1.4.

Table 2: Experimental parameters and running conditions.

Run	g1c
Running period	November 11–20, 1999
Electron-beam energy	2.445 GeV
Electron-beam polarization (average)	0.656
Tagged-photon-beam-energy range	(0.5 – 2.3) GeV
Target	liquid hydrogen (unpolarized)
Target length	178.5(5) mm
Target diameter	40 mm
Target density	$0.0711(1)$ g cm^{-3}
CLAS Torus magnetic field	1920 A
Event trigger	Level 1, with coincidence between hits in the tagger, start counter, and time-of-flight paddles
Range of run numbers	21763 – 21983
Runs used in the analysis	137

4 Data analysis

4.1 Particle and channel identification

4.1.1 Reaction vertex

The reconstructed event vertex is stored in the MVRT bank. Panels (a) to (c) of Fig. 2 show the vertex-x, -y, and -z distributions for a subset of the g1c data for which all the particle and channel identification cuts for the $\gamma p \rightarrow p\pi^+\pi^-$ reaction have been applied except for the reaction vertex. Information about the interaction vertex can help to reduce background to the $\gamma p \rightarrow p\pi^+\pi^-$ reaction. Panel (d) shows an example of a vertex-z distribution for background events in the production data at low-photon-energies ($E_\gamma < 0.9$ GeV) for which a proton and a π^- has been detected in CLAS, but where the missing mass squared of these particles is negative. The plot indicates that these background
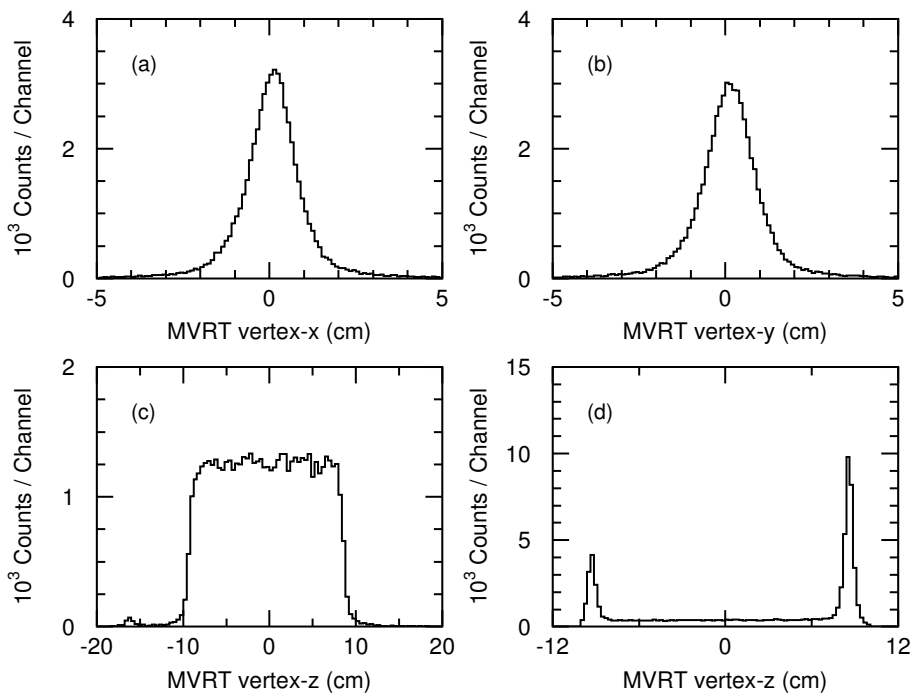

Figure 2: Vertex distributions for a subset of the $\gamma p \rightarrow p\pi^+\pi^-$ g1c data; (a), (b), and (c) for vertex-x, y, and z, respectively; (d) Vertex-z distribution for a subset of low-photon-energy background events from production data, see text.

events originate mostly from the target-entrance and -exit windows, possibly also from the target walls. To remove events from the target windows, other target structure material, or generally mistracked events, cuts on the vertex

coordinates were applied as follows:

$$-7.5 \text{ cm} < z_{\text{MVRT}} < 7.5 \text{ cm}, \tag{8}$$

$$x_{\text{MVRT}}^2 + y_{\text{MVRT}}^2 < 4 \text{ cm}^2. \tag{9}$$

Also events without proper vertex reconstruction ($z_{\text{MVRT}} \equiv 0$) have been excluded. For possible helicity-dependent photon-beam positions see Sec. 4.4.

4.1.2 Tagger and coincidence time

The coincidence time between the Tagger and CLAS is given by the event-start-time difference at the interaction point between the Tagger and the Start Counter, Δt_{TGPB}. Figure 3 shows on a logarithmic scale the distribution of tagged photons as a function of the coincidence time Δt_{TGPB}, with a central peak including the true tagger-CLAS coincidences, and accidental coincidences in a series of other peaks associated with different beam buckets and separated by 2 ns each. The raw distribution is plotted as dotted histogram. Only coincident events with one and only one tagged photon within

$$|\Delta t_{\text{TGPB}}| < 1 \text{ ns} \tag{10}$$

were chosen in the subsequent analysis. The tagged energy of that photon was taken as the photon energy for the event.

The coincidence-time distribution after applying all the $\gamma p \to p\pi^+\pi^-$ selection cuts is shown in Fig. 3 as solid histogram. The fraction of accidental coincidences of at most 1.8% within $|\Delta t_{\text{TGPB}}| < 1$ ns can be estimated from the comparison in the yields between the central peak with neighboring beam buckets. The one-photon requirement reduces this fraction of accidental coincidences in the data sample strongly, since accidental events would remain only if the "true" photon had been undetected.

4.1.3 Particle identification

The protons and pions were identified by their charge (from the curvature of the particle track), momentum (from the drift chamber tracking information), and velocity (from the time of flight and path length). The particle identification of the EVNT bank was used to preselect proton, π^+, and π^- candidates. Valid pointers to the DC, SC, and ST subsystems were additionally required for those particles. Figure 4 shows the mass-square distributions, $m^2 = p^2(\beta^{-2} - 1)$, for those particles as dashed histograms after applying the vertex and coincidence-time cuts. With the assumed mass m_0 (here $m_{\pi^\pm}$ or m_p) from that identification one gets the time difference between measured and expected times of flight:

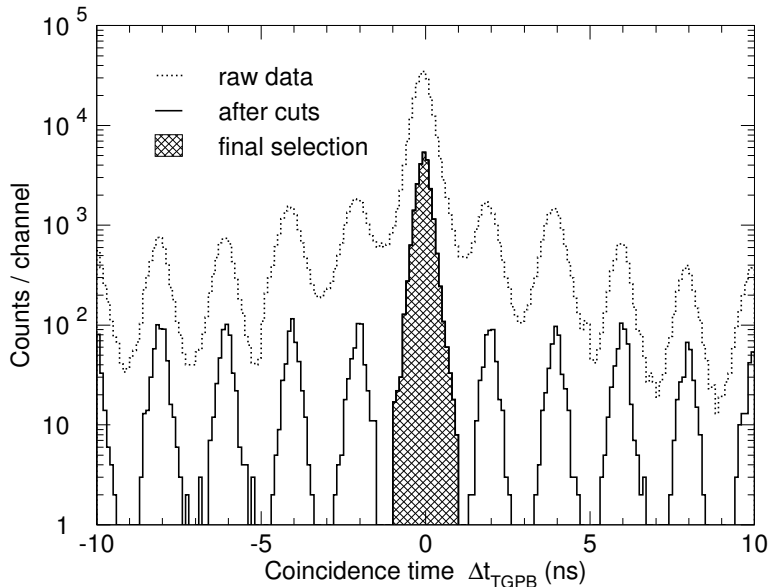$$\Delta t = \frac{l}{c} \cdot \left(\frac{1}{\beta} - \sqrt{\frac{m_0^2}{p^2} + 1} \right) . \tag{11}$$

Figure 3: Coincidence-time distribution of tagged photons for the raw data (dotted histogram) and after applying all $\gamma p \rightarrow p\pi^+\pi^-$ selection cuts (solid histogram), including the Δt_{TGPB} cut, Eq. (10). The hatched events indicate the final selection of coincidence events.

Figure 5 shows the Δt distribution for π-mesons, (a) and (b), and for protons (c). The hatched areas indicate a tight timing cut of $|\Delta t| < \delta_t$, applied to improve on the particle identification with $\delta_t = 1$ ns for π-mesons and $\delta_t = 2$ ns for protons. For both particle types δ_t is about four times the σ width of the central Δt peak. The results are shown in Fig. 4 as solid histograms. About 5% to 7% of previously identified particles were cut out, including misidentified particles at $m^2 \approx 0$. The timing cut may reject correctly identified particles, but since the timing cut does not depend on the helicity of the electron beam, this is not a concern for this analysis.

4.1.4   Reaction channel

The reaction channel of interest $(\gamma p \rightarrow p\pi^+\pi^-)$ was identified through the missing-mass technique and the detection of none but all three particles in the final state (event class 1), or the detection of none but two of the final-state particles (event classes 2–4); see Table 3. The four-momentum of an identified particle was determined from the measured three momentum and the known particle mass. The three-momentum had been corrected for energy losses in the cryogenic target material, target wall, carbon cylinder, and start counter [10].
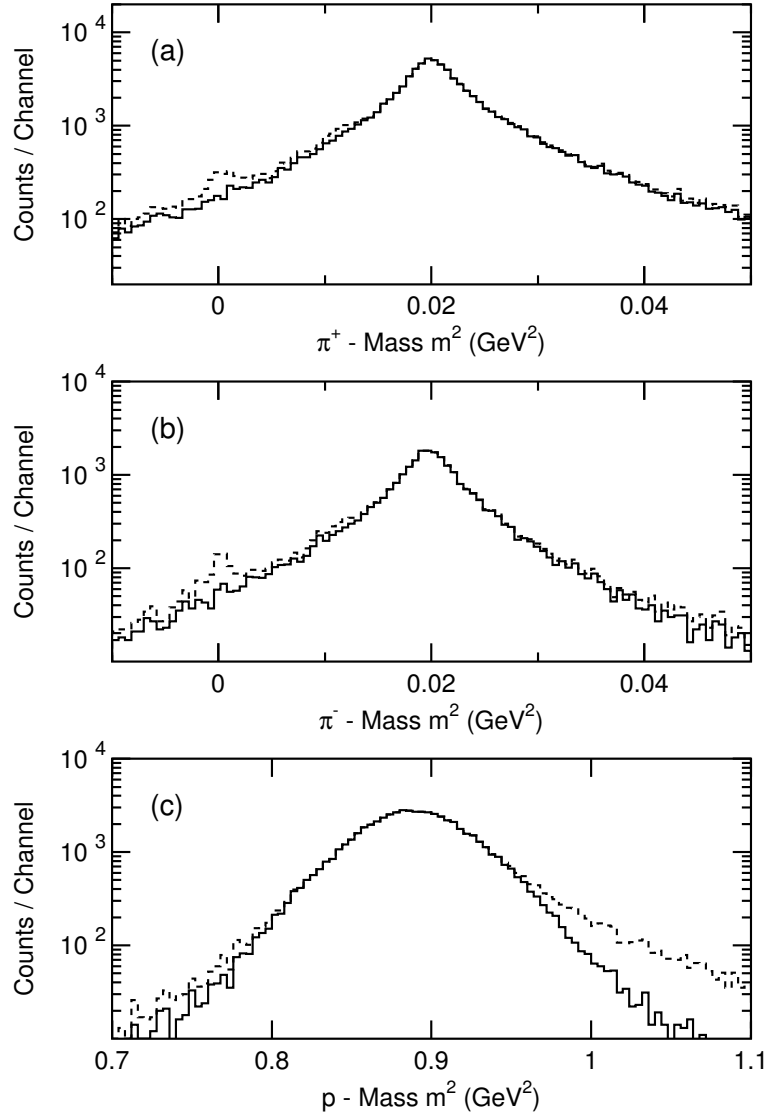
9

Figure 4: Particle mass squared for π^+-mesons (a), π^--mesons (b), and protons (c) from EVNT particle identification before (dashed histogram), and after applying an additional timing cut of $|\Delta t| < \delta_t$ (solid histogram); see Eq. (11). Data are from file a00 of run 21982.
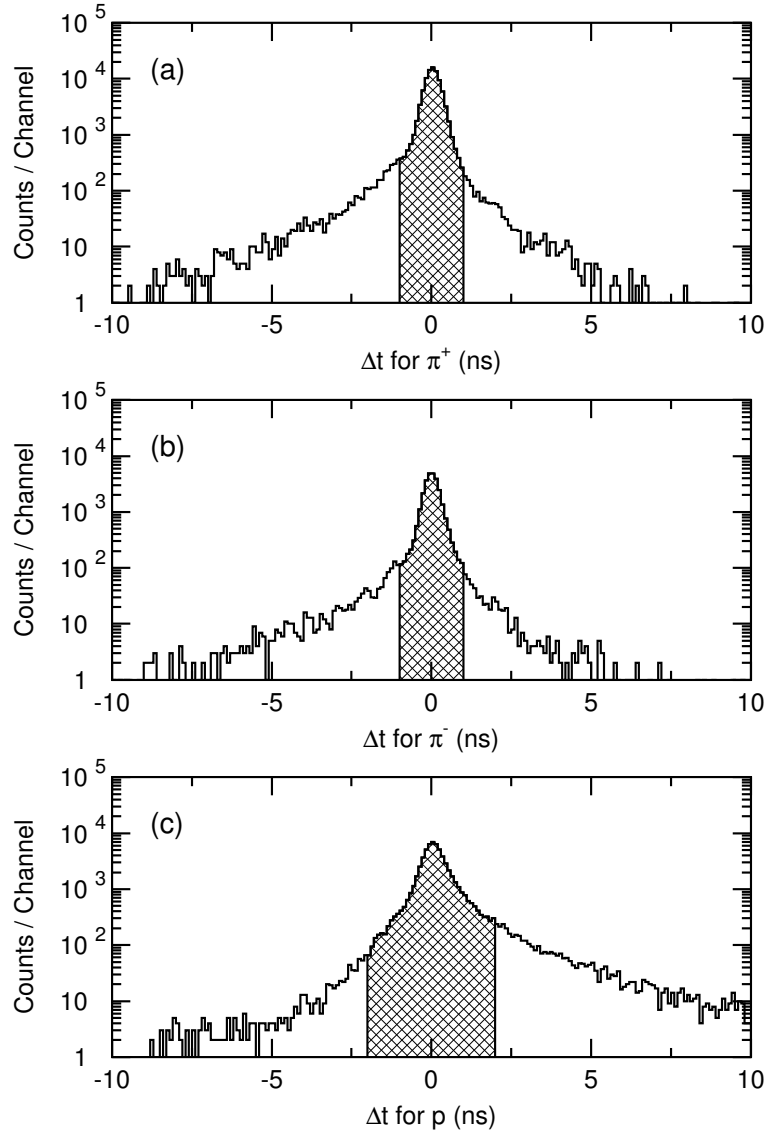
10

Figure 5: Relative flight-time distributions for π^+-mesons (a), π^--mesons (b), and protons (c). The hatched regions indicate the selected events, $|\Delta t| < \delta_t$; see Eq. (11). Data are from file a00 of run 21982.

11

The missing four-momentum is

$$x^\mu = k^\mu + P^\mu - \sum_{i=1}^{2,3} p_i^\mu \tag{12}$$

where k^μ and P^μ are the photon and proton-target four-momenta, and p_i^μ are the four-momenta of the two or three detected particles. The missing mass m_X is given by

$$m_X^2 = x^\mu x_\mu \ , \tag{13}$$

and was used to identify $\gamma p \to p\pi^+\pi^-$ events according to the selection cuts of Table 3. Figure 6 shows the m_X^2 distributions for all four event classes. The four-momentum vector x^μ from Eq. (12) was used after channel identification to complete the set of four-momentum vectors for events of classes 2, 3, or 4.

Table 3: Identification of the $\gamma p \to p\pi^+\pi^-$ channel. The total number of geometrically reconstructed particles is given by the `gpart` entry of the HEVT bank.

Class	Reconstructed particles				Missing mass	m_X^2 cut
	total	p	π^+	π^-	m_X	(GeV^2)
1	3	1	1	1	0	$-0.003 \ldots 0.001$
2	2	0	1	1	m_p	$0.70 \ldots 1.10$
3	2	1	1	0	m_{π^-}	$-0.04 \ldots 0.07$
4	2	1	0	1	m_{π^+}	$-0.04 \ldots 0.07$

There is no physical background from other reaction channels with missing masses in the regions indicated in Table 3. As stated above, background from accidental coincidences is expected to be very small (probably less than 1%). The tight particle-identification cuts and the multi particle coincidence make background contributions from misidentified particles extremely small. No hints of background are seen in Fig. 6. Thus, events passing the selection cuts and used in the analysis were assumed to be background free.

Figures 7 – 10 show examples of $\gamma p \to p\pi^+\pi^-$ event distributions. The data are from several g1c runs and are integrated over the full CLAS acceptance. The contribution of the various event classes are indicated by the hatched regions. Reconstructing an unidentified particle (event classes 2–4) greatly increases the size of the available data set. It is clear from the plots that the acceptance of CLAS has different effects on the distributions for the various event classes. In total, however, full angular coverage is accessible, even, *e.g.*, for $\cos(\theta_{\rm cm})$, where the forward and backward holes of CLAS are most prominent, as can be seen in Fig. 9.
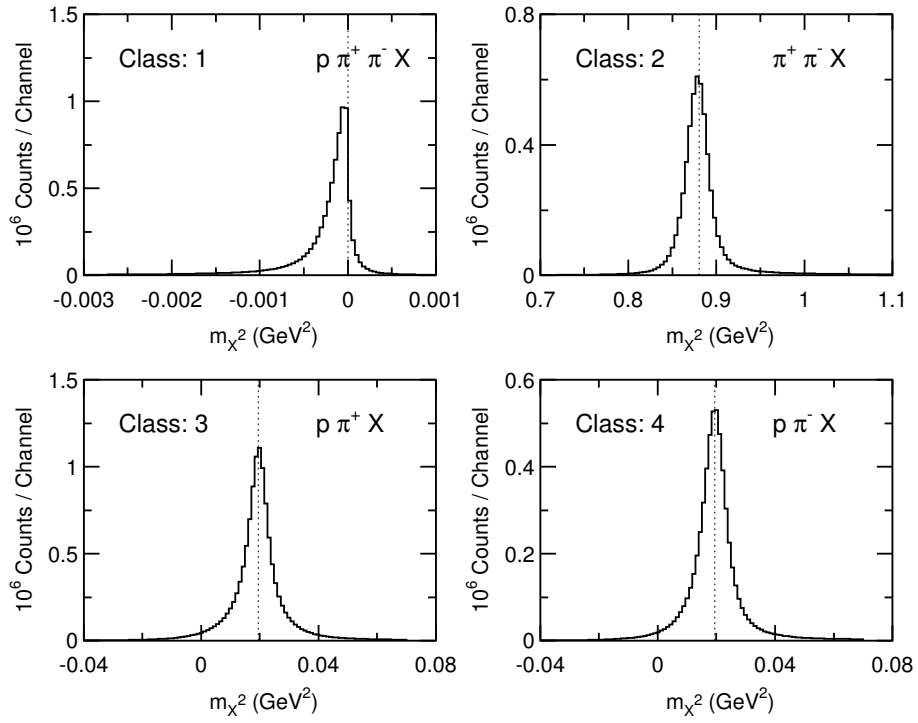
Figure 6: Missing-mass-square distributions for the four different event classes. The vertical dotted lines are at the nominal values of the mass square of the missing particle X. Indicated are the detected particles.
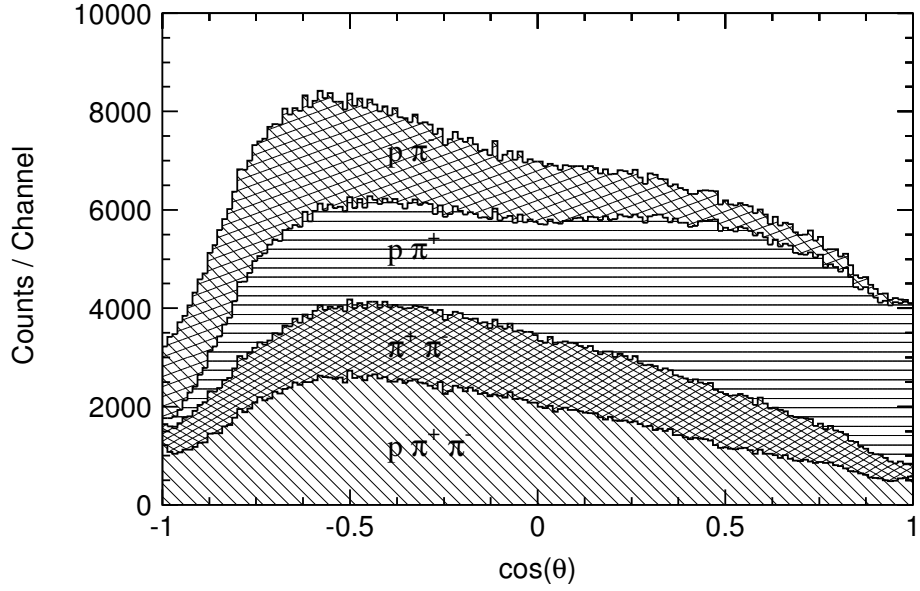
Figure 7: Summed event distribution from several runs as a function of $\cos(\theta)$ in the $p[\pi^+\pi^-]$ configuration. Contributions of the four different event classes are indicated as hatched regions along with the detected particles; from top to bottom: $p\pi^-$, $p\pi^+$, $\pi^+\pi^-$, and $p\pi^+\pi^-$.
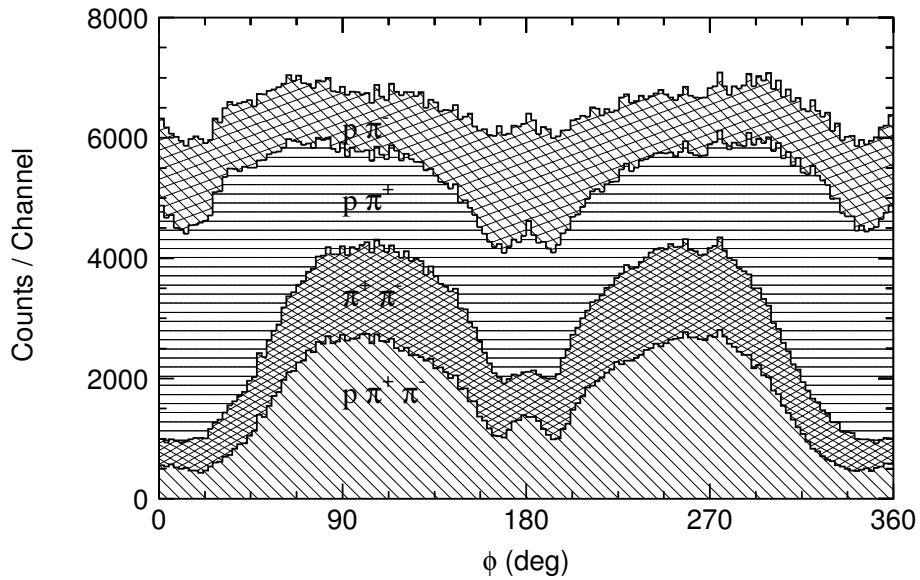

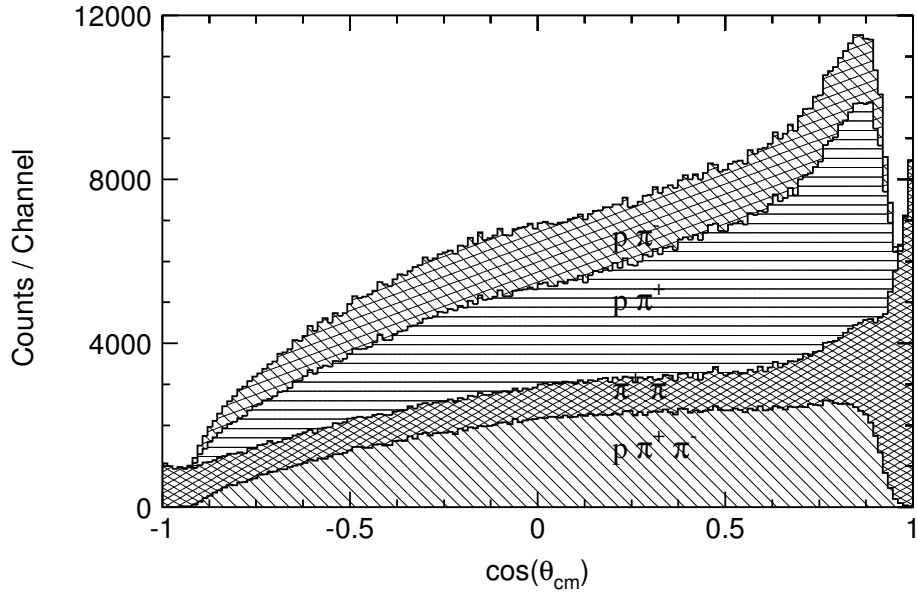Figure 8: Same as Fig. 7 for the azimuthal angle ϕ in the $p[\pi^+\pi^-]$ configuration.

14

Figure 9: Same as Fig. 7 for $\cos(\theta_{\text{cm}})$ in the $p[\pi^+\pi^-]$ configuration.
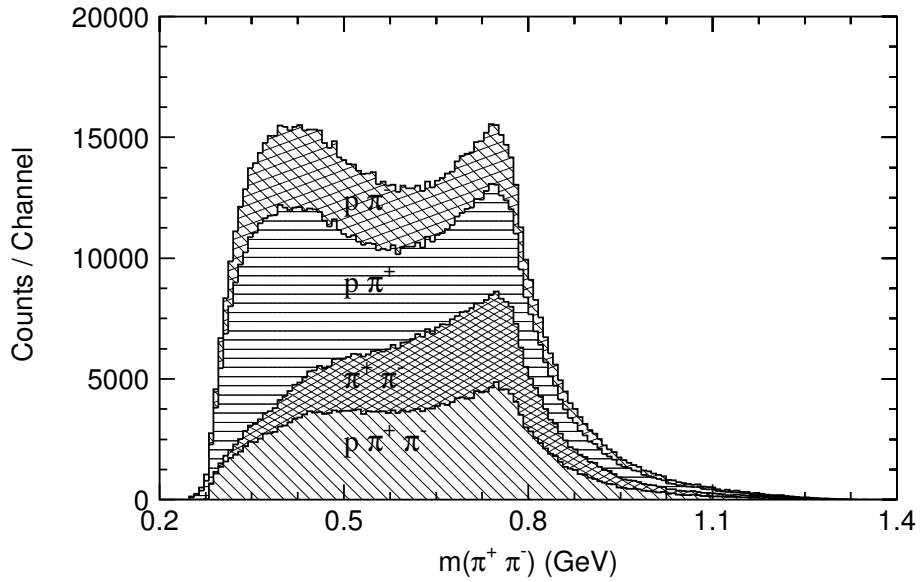

Figure 10: Same as Fig. 7 for the $\pi^+\pi^-$-invariant mass.

15

4.2 Photon-beam polarization

4.2.1 Circularly polarized bremsstrahlung

Circularly polarized photons are produced using a beam of longitudinally polarized electrons incident on the bremsstrahlung radiator. For the g1c running period a gold foil with a thickness of 10^{-4} radiation length was most often used. The degree of circular polarization of the photon beam is proportional to the electron-beam polarization P_e. In particular, with $x = E_\gamma/E_e$, the degree of circular polarization of bremsstrahlung from longitudinally polarized electrons is given by [11]

$$P_\gamma = P_e \cdot \frac{4x - x^2}{4 - 4x + 3x^2} \ ,$$
(14)

when the final electron spin is not observed and when all final electron angles are integrated out. Olsen and Maximon found that screening and Coulomb corrections do not have any significant influence on the circular polarization, and thus they are not included in Eq. (14).
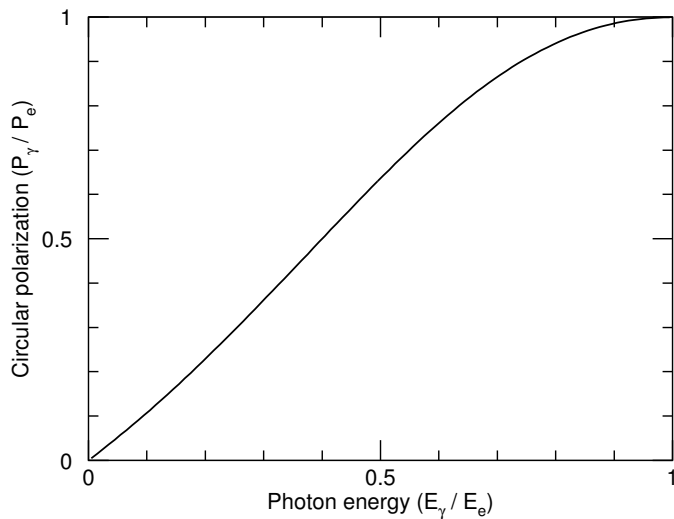

Figure 11: Circular polarization of the photon beam as a function of photon energy.

Table 4 summarizes the Møller measurements of the electron-beam polarization. In this analysis a mean value of 65.6% with an uncertainty of 1.5% is used for the degree of the electron-beam polarization.

4.2.2 Electron-beam helicity

The longitudinal polarization of the electron beam was flipped pseudo-randomly with 30 sequences of helicity $(+, -)$ or $(-, +)$ signals per second; see Fig. 14.

Table 4: Møller measurements of the electron-beam polarization.

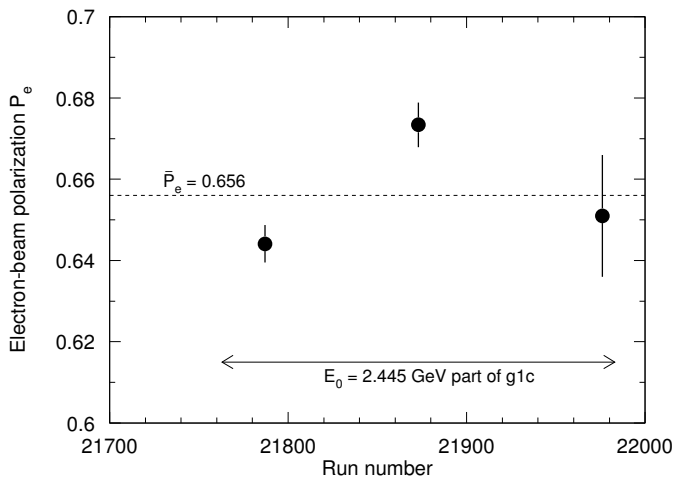| Date	e-log entry	Beam polarization P_e	Run number
Nov. 13, 1999	6943	$64.41\% \pm 0.46\%$	21787
Nov. 16, 1999	6964	$67.34\% \pm 0.55\%$	21873
Nov. 22, 1999	7034	$65.1\% \pm 1.5\%$	21976

Figure 12: Møller measurements of the electron-beam polarization.

Occasionally a $\lambda/2$ plate is inserted in the circularly-polarized laser beam of the electron gun to reverse helicities and provide for systematic checks. The $\lambda/2$ plate position for the g1c run period has been recorded in the EPICS data base. Over the entire period the $\lambda/2$ plate was out. Experimental asymmetries in each run are experimental checks of the sign of the beam polarization over time. Figure 13 shows $\sum h \sin(\phi) / \sum \sin^2(\phi)$ as a function of run number.[1] The stability of the setup and thus the correspondence between helicity bit 16 and the electron-beam helicity, see Tab. 5, is confirmed by the constant asymmetry value indicated by the dashed line.

The electron-beam helicity information is stored in the level1-trigger-latch word (TGBI bank). Bit 15 contains the helicity clock. A high state of the helicity-clock bit indicates the start of a new helicity-signal sequence. Bit 16 is the helicity-state bit. It indicates the sign of the electron-beam polarization (for $\lambda/2$ plate in OUT position); see Table 5, and the CLAS analysis note [12].

---

[1] The sum was taken over events within 1.5 GeV $< W <$ 1.9 GeV, and ϕ as the azimuthal angle in $p[\pi^+, \pi^-]$ configuration in the Adair system.
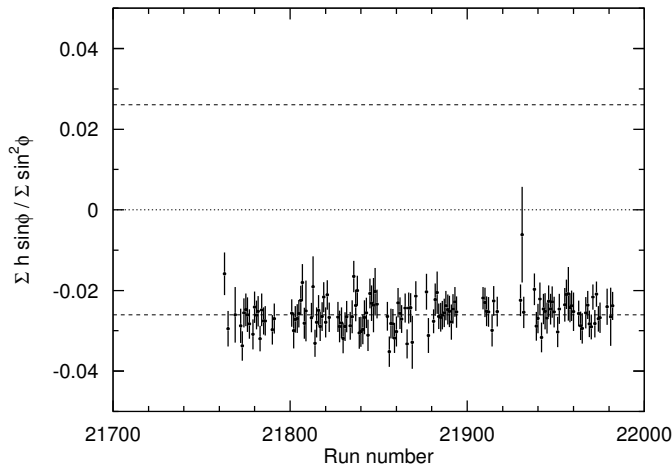
Figure 13: Experimental asymmetry by run for all runs used in this analysis; see text. The lower dashed line is a fit to the data, the upper dashed line corresponds to a change in sign, which could occur from a change in the half-wave-plate position. No sign change is observed during the experiment.

Table 5: Helicity signal from the TGBI-bank `latch1` for the two half-wave-plate positions.

| TGBI `latch1` | Beam helicity | |
bit-16	$\lambda/2$ (OUT)	$\lambda/2$ (IN)
1	$+$	$-$
0	$-$	$+$

4.2.3 Beam-charge asymmetry

Over time, the photon-beam flux for both helicity states should be identical on average. Small beam-charge asymmetries of the electron beam, however, can cause instrumental asymmetries in the observed $\gamma p \to p \pi^+ \pi^-$ asymmetries, and need to be taken into account. This was done by considering the luminosities for helicity-plus and -minus events:

$$\mathcal{L}^{\pm} = \alpha^{\pm} \mathcal{L} \,, \tag{15}$$

xp where $\mathcal{L}$ is the total luminosity, and the values for

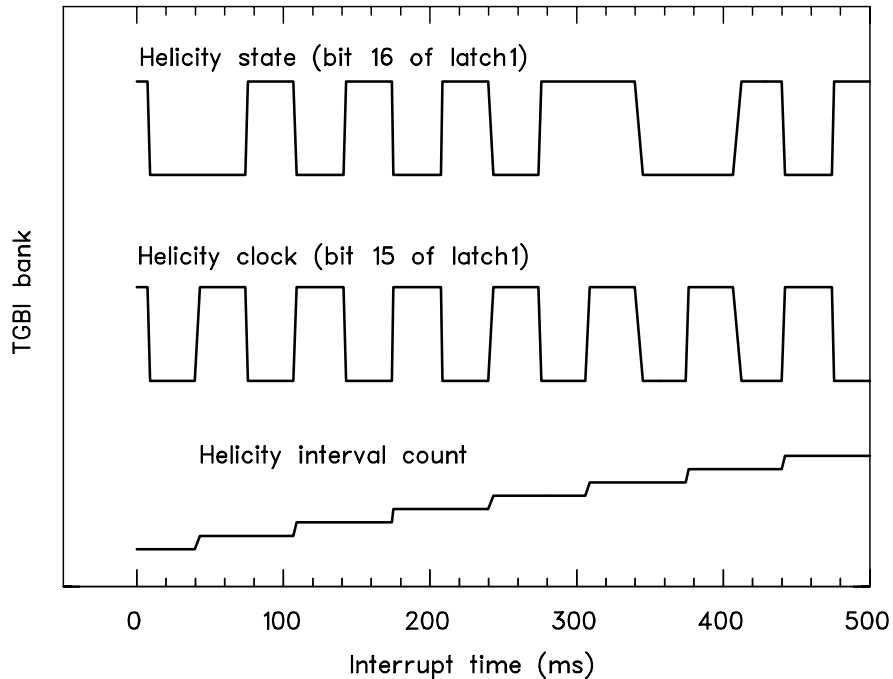$$\alpha^{\pm} = \frac{1}{2} \left(1 \pm \bar{a}_c \right) \tag{16}$$

18

Figure 14: TGBI bank information from `latch1` and `interrupt_time` of the first 500 ms of the data from one particular g1c file.

depend on the mean value of the electron-beam-charge asymmetry $\bar{a}_c$.

The beam-charge asymmetry a_c was experimentally derived from the sum $N_\pi^\pm$ of observed single-pion photoproduction events from both the $\gamma p \rightarrow p\pi^0$ and $n\pi^+$ reactions for the two helicity states:

$$a_c = \frac{N_\pi^+ - N_\pi^-}{N_\pi^+ + N_\pi^-} \ .$$

(17)

In these two-body–to–two-body reactions, and with the unpolarized proton target, there is no cross-section difference for the two helicity states. Any observed asymmetry a_c in the yield is thus instrumental. Figure 15 shows a histogram of a_c for the g1c runs used in this analysis. The mean charge asymmetry $\bar{a}_c = -0.0043 \pm 0.0001$ follows from the sum of the events in all runs.

4.3   Cross-section asymmetry

The experimental value for the helicity-dependent cross-section asymmetry for a specific phase-space volume $\Delta\tau$ is given by

$$A^{\mathrm{exp}}(\Delta\tau) = \frac{1}{\bar{P}_\gamma} \cdot \frac{Y^+ - Y^-}{Y^+ + Y^-} \ .$$
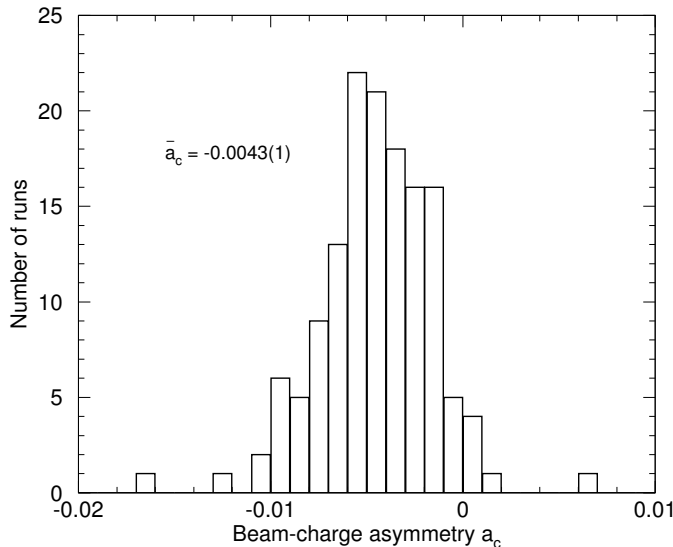
(18)

19

Figure 15: Distribution of beam-charge asymmetries for the analyzed runs.

The variable τ represents collectively all the variables necessary to have a complete description of the final state, e.g., photon-beam energy and particle momenta. Here, $Y^\pm = N^\pm/\alpha^\pm$ are the total number of $\gamma p \to p\pi^+\pi^-$ events for the two helicity states observed within $\Delta\tau$ and corrected for the electron-beam-charge asymmetry, and $\bar{P}_\gamma$ is the mean value of the circular polarization; see Eq. (14):

$$\bar{P}_\gamma = \frac{1}{N^+ + N^-} \sum_{i \in \Delta\tau} P_\gamma(E_{\gamma,i}) .$$ (19)

The phase-space volume can be, the full CLAS acceptance or any subset thereof defined by kinematical constraints.

Equation (18) provides for the link between the measured count-rate asymmetry and the physical helicity asymmetry A, given by Eq. (2). The total numbers of observed counts are

$$N^\pm = \int_{\Delta\tau} \epsilon(\tau)\mathcal{L}^\pm\sigma(\tau,\pm)d\tau ,$$ (20)

where ϵ is the product of acceptance and detection efficiency, and the cross section σ is given by Eq. (1). The argument τ is generic for all quantities which may vary within the phase space volume $\Delta\tau$. For the normalized yields using Eqs. (2) and (15), one obtains

$$Y^\pm = \int_{\Delta\tau} \epsilon(\tau)\mathcal{L}\Sigma(\tau)\left[1 \pm P_\gamma(\tau)A(\tau)\right]d\tau ,$$ (21)

20

and together with Eq. (18)

$$A^{\text{exp}} \quad = \quad \frac{1}{\bar{P}_\gamma} \frac{\int_{\Delta\tau} \epsilon(\tau)\Sigma(\tau)P_\gamma(\tau)A(\tau)d\tau}{\int_{\Delta\tau} \epsilon(\tau)\Sigma(\tau)d\tau} \quad (22)$$

$$\approx \quad \frac{\sum_{i\in\Delta\tau} P_\gamma(\tau_i)A(\tau_i)}{\sum_{i\in\Delta\tau} P_\gamma(\tau_i)} \ . \quad (23)$$

Where the sum is running over all events i observed in the phase-space volume $\Delta\tau$. Thus, A^{exp} is the event- and polarization-weighted mean value of the helicity asymmetry averaged over the observed event sample within the phase-space volume $\Delta\tau$. The degree of circular polarization $P_\gamma(\tau_i)$ changes with photon-beam energy and is thus also dependent on the event kinematics τ_i. Equation (23) provides a way to compare the experimental data with results of model calculations, by performing the same averaging with the calculated asymmetries.

The cross-section asymmetry is independent of the experimental luminosity (photon flux, tagging efficiency, target density). Furthermore, since the product of the CLAS acceptance and efficiency is independent of the photon-beam helicity, it too does not enter into the determination of A^{exp}. The value of A^{exp} is exactly independent of ϵ if the phase-space volume is sufficiently small, so that ϵ is constant over $\Delta\tau$. A varying ϵ affects the event topology and mean kinematics and thus influences the event sample used to determine $A^{\text{exp}}(\Delta\tau)$. In that case, the experimental event sample within $\Delta\tau$ — not the actual value of ϵ — needs to be taken into account when comparing A^{exp} with model calculations of the asymmetry; see Eq. (23).

An example of an experimental cross-section asymmetry is shown in Fig. 16. This is a typical example, except for the fact that particularly large asymmetries have been observed in this phase-space volume. Panels (a) and (b) show the ϕ angular distributions of the $\gamma p \rightarrow p\pi^+\pi^-$ helicity-plus and -minus events, respectively. The phase-space volume for this event sample is defined by the CLAS acceptance and $W \in [1.68, 1.72]$ GeV, $\cos(\theta_{\text{cm}}) \in [-1.0, -0.3]$, $\cos(\theta) \in [-0.50, -0.25]$. The yield distributions obey approximately the symmetry relation

$$N^+(\phi) \approx N^-(-\phi) \ . \quad (24)$$

Panel (c) shows the resulting helicity asymmetry following Eq. (18). The asymmetry is corrected for the beam-charge asymmetry and the photon polarization. It is fitted with a series of sine and cosine functions,

$$A^{\text{exp}}(\phi) = \sum_{k=1}^{n} a_k \sin(k\phi) + \sum_{k=0}^{n} b_k \cos(k\phi) \ , \quad (25)$$

shown as solid curve in Fig. 16(c) for $n = 3$. All cosine-Fourier coefficients are consistent with zero and the dashed curve fits the data equally well with only sine terms up to the order of $n = 2$. The fit results are summarized in Table 6. This indicates that $A(\phi)$ is an odd function. Additionally, the cross-section
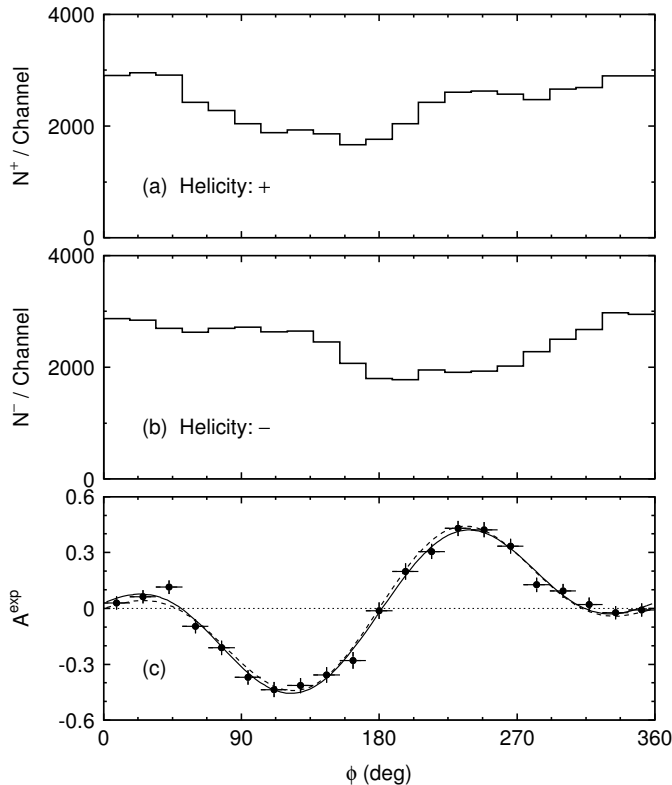
Figure 16: Example of ϕ angular distributions in the helicity frame of helicity-plus events (a), and helicity-minus events (b), as well as the resulting cross-section asymmetry (c). The data were selected according to $W \in [1.68, 1.72]$ GeV, $\cos(\theta_{\mathrm{cm}}) \in [-1, -0.3]$, $\cos(\theta) \in [-0.50, -0.25]$, and otherwise integrated over the CLAS acceptance. The azimuthal angle ϕ is given in the $p[\pi^+, \pi^-]$ configuration. The solid curve is a fit of Eq. (25) with $n = 3$ to the data; the dashed curve is for $n = 2$ and $b_k = 0$.

asymmetries vanish for $\phi = 0$ and $\phi = 180°$ when all particles are coplanar. Indeed, this is expected from parity conservation. $A(\phi)$ being an odd function is equivalent to Eq. (24).

It is important to note that experimentally, even-function contributions may enter into the angular distributions. For that to happen, three effects have to coincide. Firstly, the considered phase-space volume has to be large enough to allow for substantial changes of the CLAS acceptance (or detector efficiency) within that phase-space volume. Secondly, these acceptance changes have to be angular dependent, such that the mean kinematics of the data varies with ϕ. Thirdly, the change in kinematics has to yield to a change in asymmetry. Indications for such an effect are not seen in the angular distribution of Fig. 16(c),

Table 6: Fit results for the two different fits to the 21 data points of the angular distribution of the helicity asymmetry in Fig. 16(c).

Parameters	Fit-1	Fit-2
χ^2	14.5	20.4
d.o.f	14	19
a_1	-0.292 ± 0.012	-0.291 ± 0.012
a_2	0.214 ± 0.012	0.215 ± 0.012
a_3	0.011 ± 0.012	0
b_0	-0.003 ± 0.009	0
b_1	0.025 ± 0.012	0
b_2	0.007 ± 0.012	0
b_3	0.002 ± 0.012	0

nor in any other case shown below in this report. Furthermore, this effect is not a concern for this analysis, since the interpretation of the data is done by comparing it with a model, and in this comparison the actual kinematics of the event sample is taken into account.

4.4 Systematic uncertainties

The beam helicity is flipped in the injector of the electron accelerator. If this imposes any helicity dependence on the electron-beam orbit, one may speculate that this is carried over through the mean photon-beam position and the reaction vertex to the kinematical variables of the $\gamma p \to p\pi^+\pi^-$ reaction, finally introducing instrumental asymmetries.

However, no such effects were observed. Figure 17 shows the helicity asymmetries for the full $\gamma p \to p\pi^+\pi^-$ data set as a function of the three vertex coordinates as given by the MVRT bank. Shown are the raw count-rate asymmetries (open circles). As expected, these asymmetries are low, and reflect mostly the beam-charge asymmetry a_c. After correcting for this effect the asymmetries are close to zero (filled circles). They show no dependence on any of the reaction-vertex coordinates, as shown by noting that the fit of a constant to the 48 data points yields favorable values for χ^2 per degree of freedom of 0.8, 1.3, and 0.8 for the x, y, and z distributions, respectively. Their constants are summarized along with the beam-charge asymmetry in Table 7. Instrumental asymmetries due to helicity-dependent beam positions are smaller than 0.1%.

The experimental systematic uncertainties are dominated by the knowledge

Table 7: Mean helicity asymmetries for the full $\gamma p \to p\pi^+\pi^-$ data set.

Beam-charge asymmetry	$\bar{a}_c$	-0.0043 ± 0.0001
Raw event asymmetry	$\frac{N^+ - N^-}{N^+ + N^-}$	-0.0038 ± 0.0002
Event asymmetry corrected for a_c	$\frac{Y^+ - Y^-}{Y^+ + Y^-}$	0.0005 ± 0.0002

of the beam polarization of the circularly polarized photon beam. Contributions to the systematic uncertainties are summarized in Table 8.

Table 8: Systematic contributions to the uncertainties in A^{exp}. The values are given as standard deviations, u.

Contribution	$u(A^{\mathrm{exp}})$	$u(A^{\mathrm{exp}})/A^{\mathrm{exp}}$
Circular polarization of photon beam		1.5%
Electron beam-charge asymmetry	$< 0.1\%$	
Photon beam position	$< 0.1\%$	

5 Results

5.1 Examples of angular distributions

Figures 18, 19, and 20 show examples of ϕ angular distributions of the cross-section asymmetry for twelve equal center-of-mass-energy bins from 1.35 GeV to 2.30 GeV for the three configurations $p[\pi^+, \pi^-]$, $\pi^-[p, \pi^+]$, and $\pi^+[\pi^-, p]$, respectively. The data are integrated over the CLAS acceptance. They reveal asymmetries with a strong energy dependence in amplitude as well as structure. Fits of Eq. (25) to the data with $n = 5$ and $b_k = 0$ are shown as solid curves. Figures 21 to 24 show additional differential angular distributions, where the center-of-mass energy has been kept fixed at $W = (1.68 - 1.72)$ GeV and the data have been binned in other kinematical variables, namely, $\cos(\theta_{\mathrm{cm}})$, $\cos(\theta)$, and the invariant masses $m(\pi^+, \pi^-)$ and $m(p, \pi^+)$.
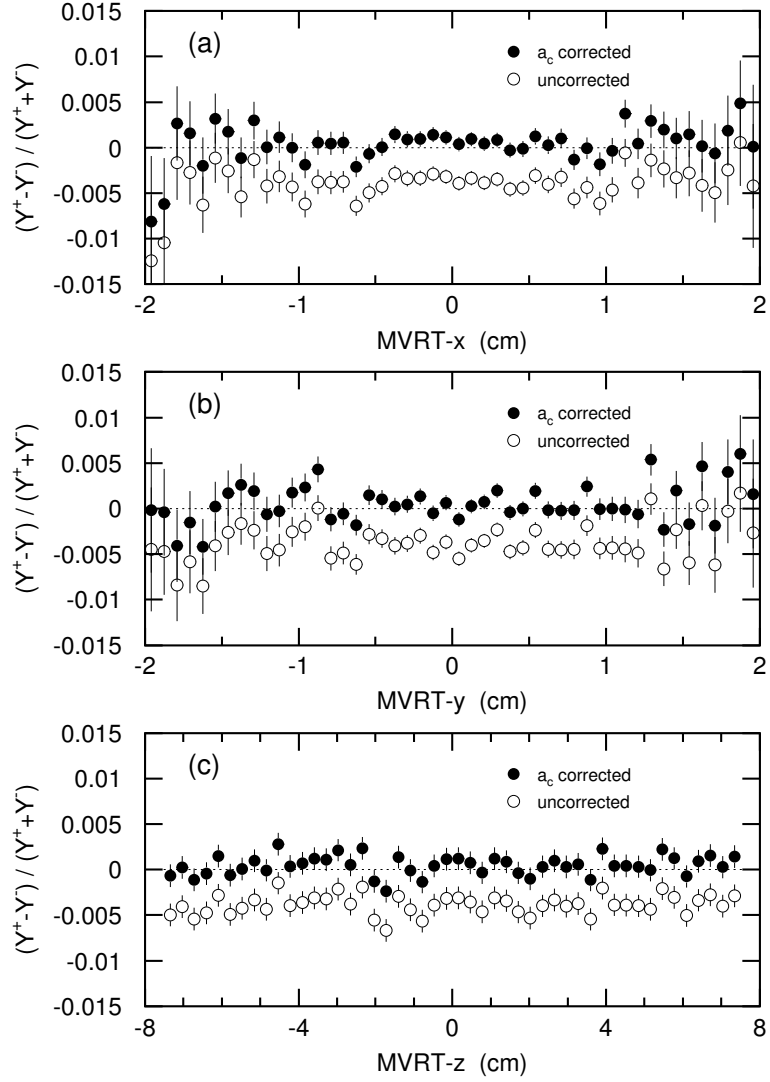
Figure 17: Helicity asymmetries of the $\gamma p \to p\pi^+\pi^-$ data set corrected for the beam-charge asymmetry (filled circles), and raw, uncorrected count-rate asymmetries (open circles) as a function of the MVRT vertex coordinates x (a), y (b), and z (c).
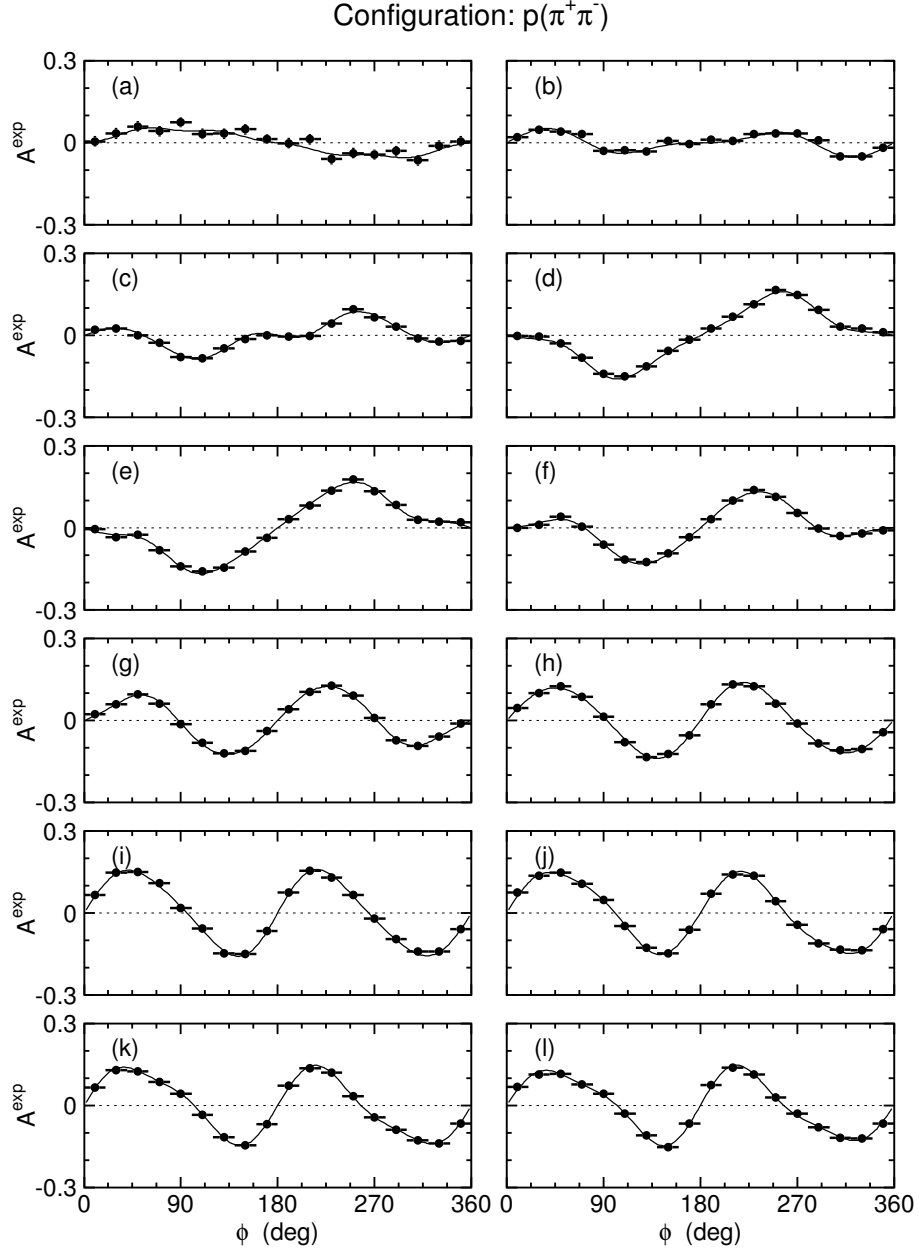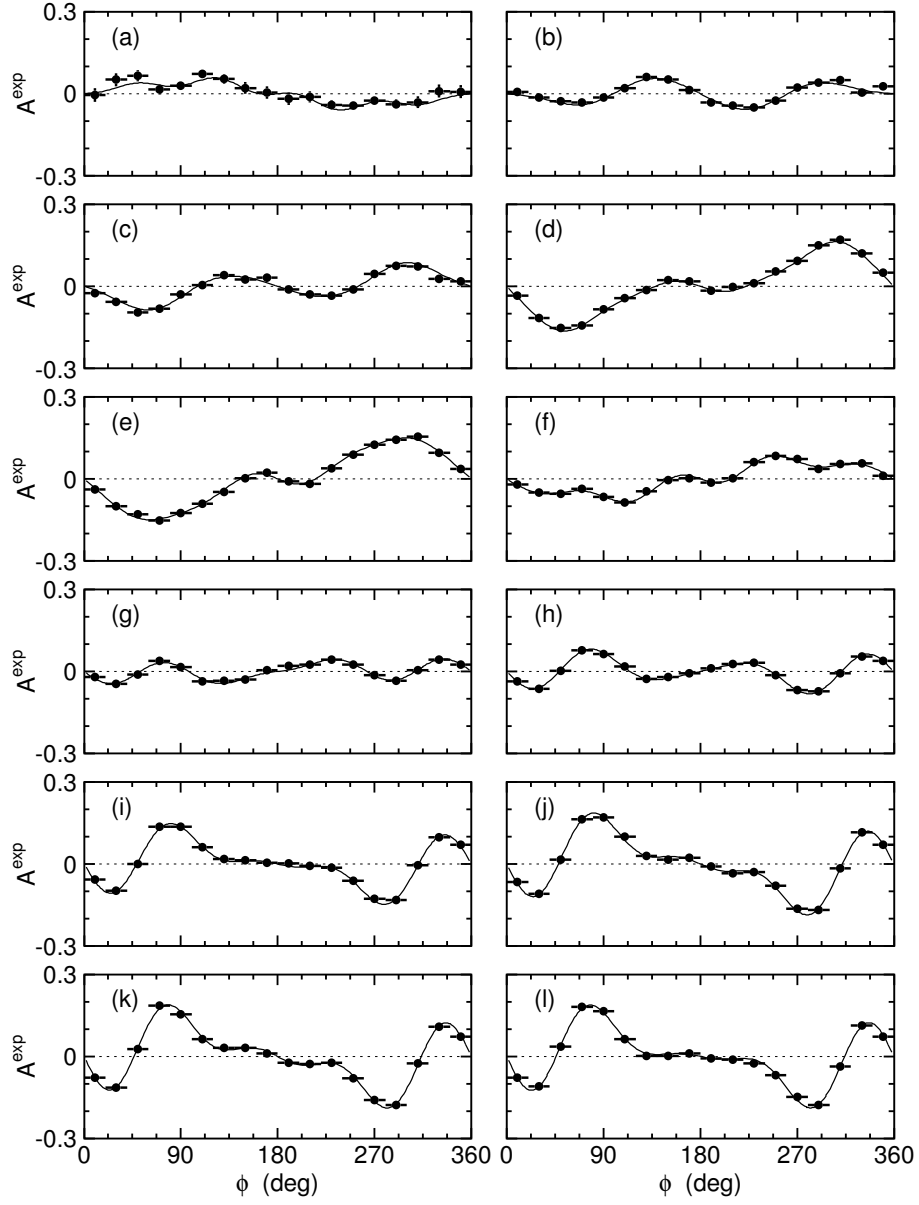
Configuration: p($\pi^+\pi^-$)

Figure 18: Azimuthal angular distributions of the cross-section asymmetry for twelve equal energy bins between $W = 1.35$ GeV and 2.30 GeV. The angle ϕ is taken in the configuration $p[\pi^+\pi^-]$; data are integrated over the full CLAS acceptance. The solid lines are fits of Eq. (25) to the data with $n = 5$ and $b_k = 0$.
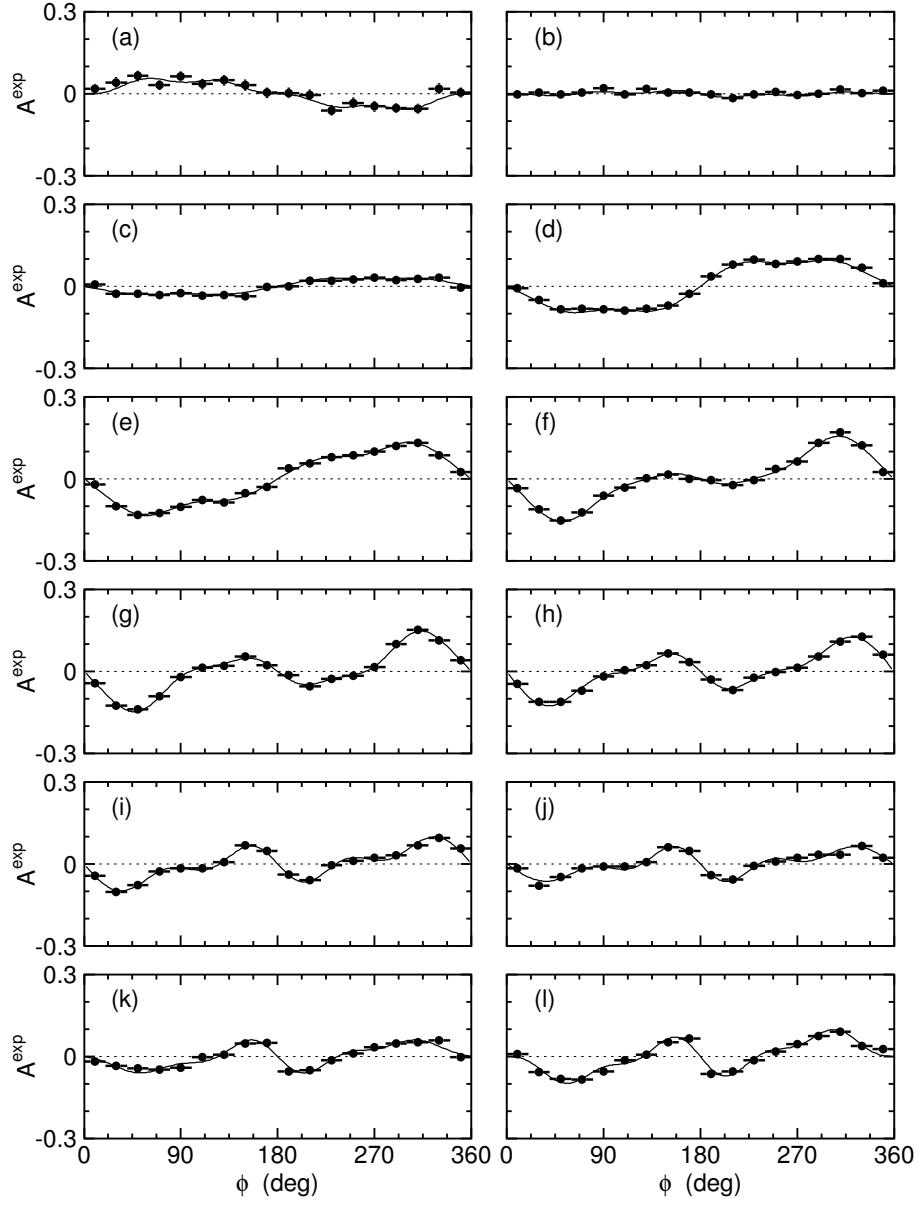
Configuration: $\pi^-(p\pi^+)$

Figure 19: Azimuthal angular distributions of the cross-section asymmetry for twelve equal energy bins between $W = 1.35$ GeV and 2.30 GeV. The angle ϕ is taken in the configuration $\pi^-[p, \pi^+]$; data are integrated over the full CLAS acceptance. The solid lines are fits of Eq. (25) to the data with $n = 5$ and $b_k = 0$.

27

Figure 20: Azimuthal angular distributions of the cross-section asymmetry for twelve equal energy bins between $W = 1.35$ GeV and 2.30 GeV. The angle ϕ is taken in the configuration $\pi^+[\pi^-, p]$; data are integrated over the full CLAS acceptance. The solid lines are fits of Eq. (25) to the data with $n = 5$ and $b_k = 0$.
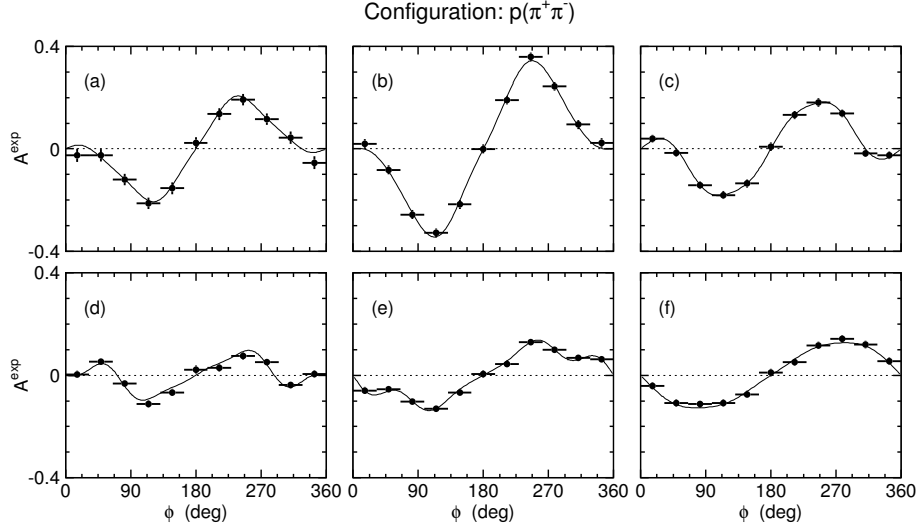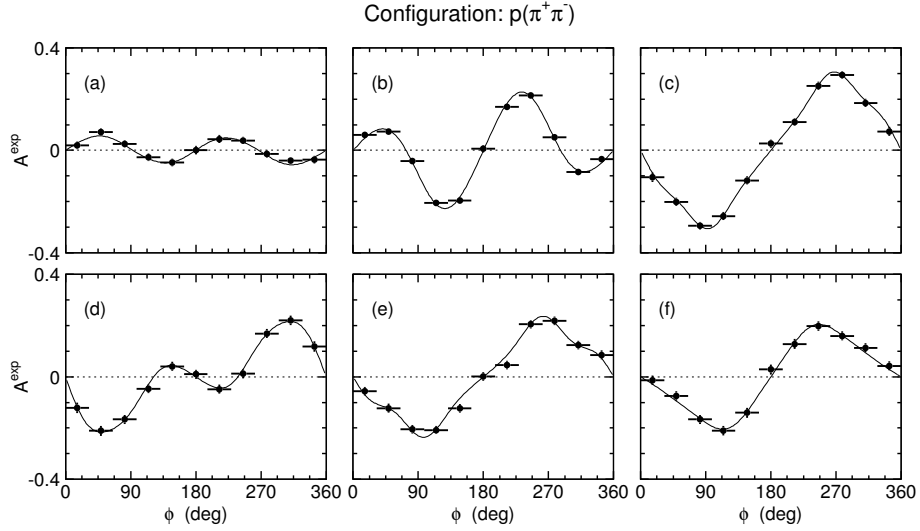
Figure 21: CLAS-integrated azimuthal angular distributions of the cross-section asymmetry for the energy bin $W = (1.68 - 1.72)$ GeV for six equal angular bins in $\cos(\theta_{\mathrm{cm}})$, between -1 and $+1$, from (a) to (f). The solid lines are fits of Eq. (25) to the data with $n = 5$ and $b_k = 0$.

Figure 22: CLAS integrated azimuthal angular distribution of the cross-section asymmetry for the energy bin $W = (1.68 - 1.72)$ GeV for six equal angular bins in $\cos(\theta)$, between -1 and $+1$, from (a) to (f). The solid lines are fits of Eq. (25) to the data with $n = 5$ and $b_k = 0$.
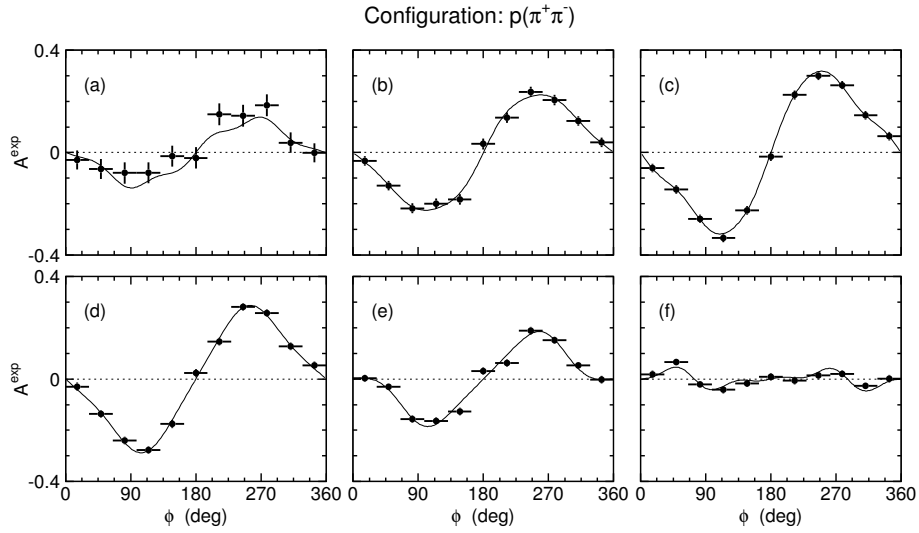
Figure 23: CLAS integrated azimuthal angular distribution of the cross-section asymmetry for the energy bin $W = (1.68 - 1.72)$ GeV for six equal energy bins in the $\pi^+\pi^-$-invariant mass between 0.25 GeV and 0.70 GeV, from (a) to (f). The solid lines are fits of Eq. (25) to the data with $n = 5$ and $b_k = 0$.
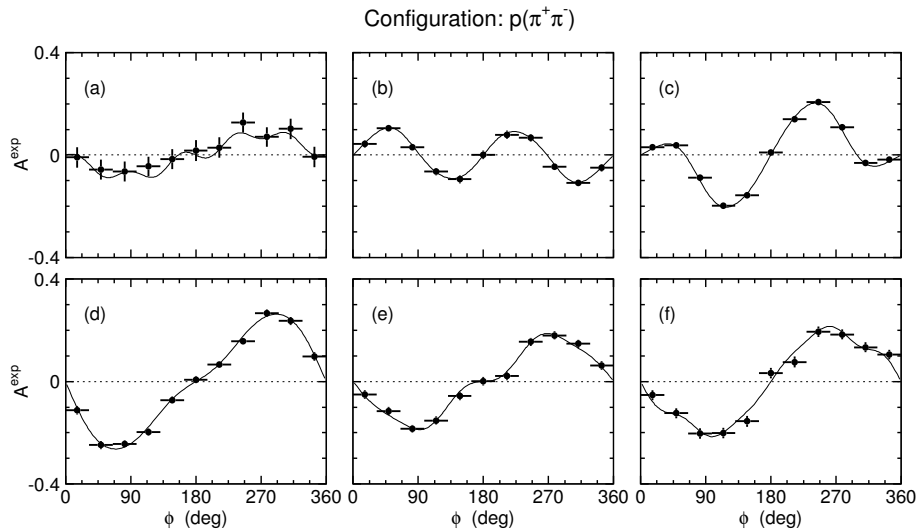

Figure 24: CLAS integrated azimuthal angular distribution of the cross-section asymmetry for the energy bin $W = (1.68 - 1.72)$ GeV for six equal energy bins in the $p\pi^+$-invariant mass between 1.05 GeV and 1.50 GeV, from (a) to (f). The solid lines are fits of Eq. (25) to the data with $n = 5$ and $b_k = 0$.

30

5.2 Examples of Fourier distributions

A way to study the energy dependence of the cross-section asymmetries is to look into the W dependence of the Fourier coefficients. Figures 25, 26, and 27 show the energy dependence of the parameters a_1 to a_4 for the fully CLAS-integrated data in the $p[\pi^+, \pi^-]$ (filled circles), $\pi^-[p, \pi^+]$ (open circles), and $\pi^+[\pi^-, p]$ (filled triangles) configurations. The figures are given for the various choices of the z axis according to the helicity (Fig. 25), Gottfried-Jackson (Fig. 26), and Adiar (Fig. 27) frames; see Table 1. Most striking is the good agreement among the three different cases for the a_1 term in the Adair system over the entire covered W range. This can be understood from momentum conservation which makes the $\sin\phi$ values for all three different configurations have the same sign (not value) in the Adair system. The a_1 and a_2 terms show in all cases the strongest energy dependence. This is not surprising, given that the $\sin\phi$ and $\sin 2\phi$ terms are govern the typical decay angular distribution W^3; Eq. (7). Nonzero coefficients a_3 and a_4 can come trivially from the *phi* dependence of the W^0, which is the denominator of the cross-section asymmetry, $A = W^3/W^0$.

Subsequent analyses will try to single out certain event samples to emphasize specific reaction channels, when comparing the experimental asymmetries with the data. As an example, Fig. 28 shows a scatter plot of the data as a function of the $p\pi^+$ invariant mass (with a clustering of events close to the mass of the Δ^{++} at 1.23 GeV), and the $\pi^+\pi^-$ invariant mass (with a clustering of events close to the ρ mass at 0.77 GeV). The boxes select events with large contributions from the $\Delta\pi$ and ρN channels, respectively; this is for reference only.

The energy dependence of the a_1 and a_2 Fourier coefficients of the observed angular distributions for the $p[\pi^+, \pi^-]$ configuration is shown in Fig. 29(a) for the full data set (filled circles), for the Δ events (open circles), and for the ρ events (filled triangles), as denoted in Fig. 28. Figure 29(b) shows the ρ events with additional angular cuts, namely, for data with $\cos(\theta_{cm}) < -0.5$ (filled circles), $-0.1 < \cos(\theta_{cm}) < -0.1$ (open circles), and $\cos(\theta_{cm}) > 0.7$ (filled triangles), showing the large variation with θ_{cm}.
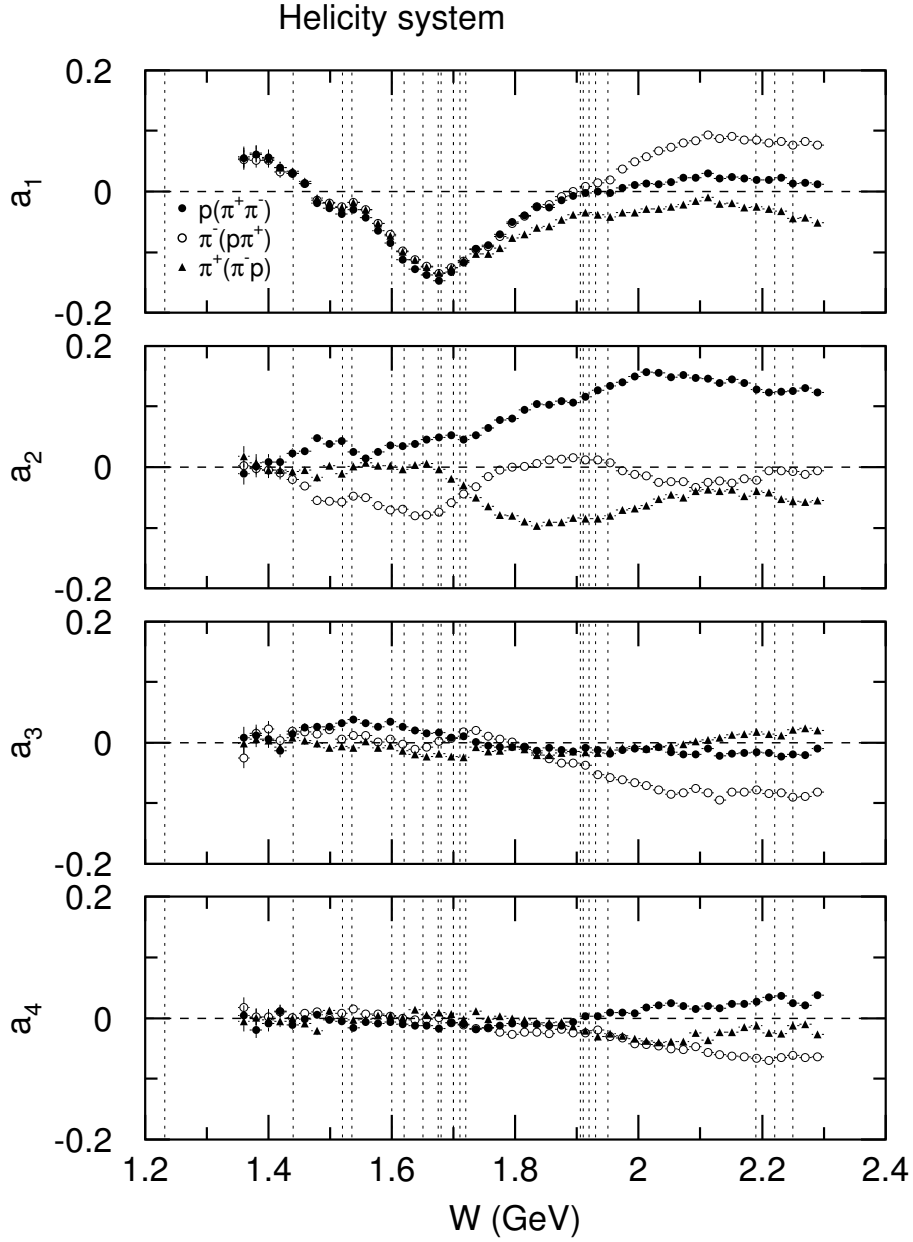
Figure 25: Fourier components of the $\gamma p \to p\pi^+\pi^-$ cross-section asymmetry in the helicity system as a function of the γp center-of-mass energy. The data for the various configurations were integrated over the full CLAS acceptance. The vertical lines indicate the masses of 3- and 4-star resonances [1].
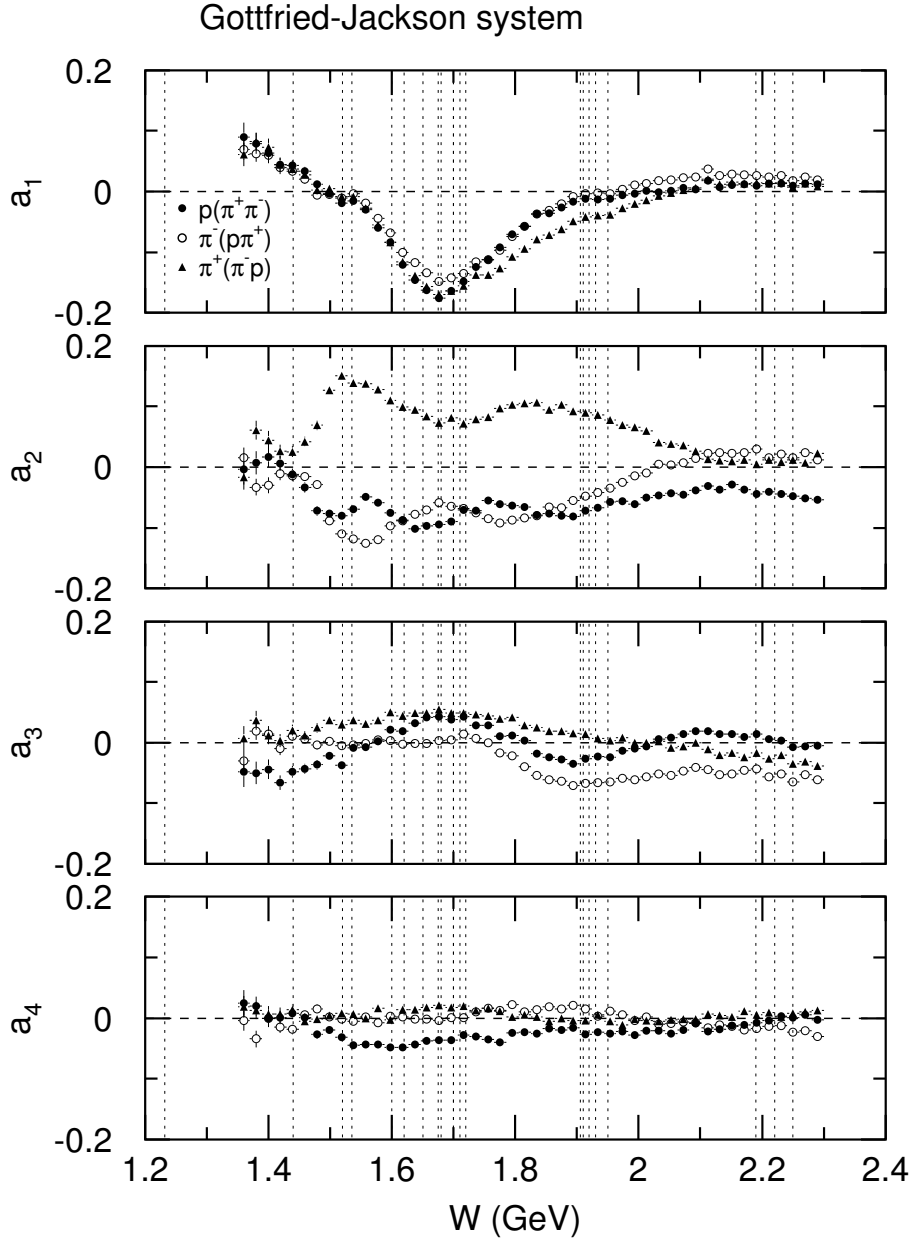
Figure 26: Fourier components of the $\gamma p \to p\pi^+\pi^-$ cross-section asymmetry in the Gottfried-Jackson system as a function of the γp center-of-mass energy. The data for the various configurations were integrated over the full CLAS acceptance. The vertical lines indicate the masses of 3- and 4-star resonances [1].
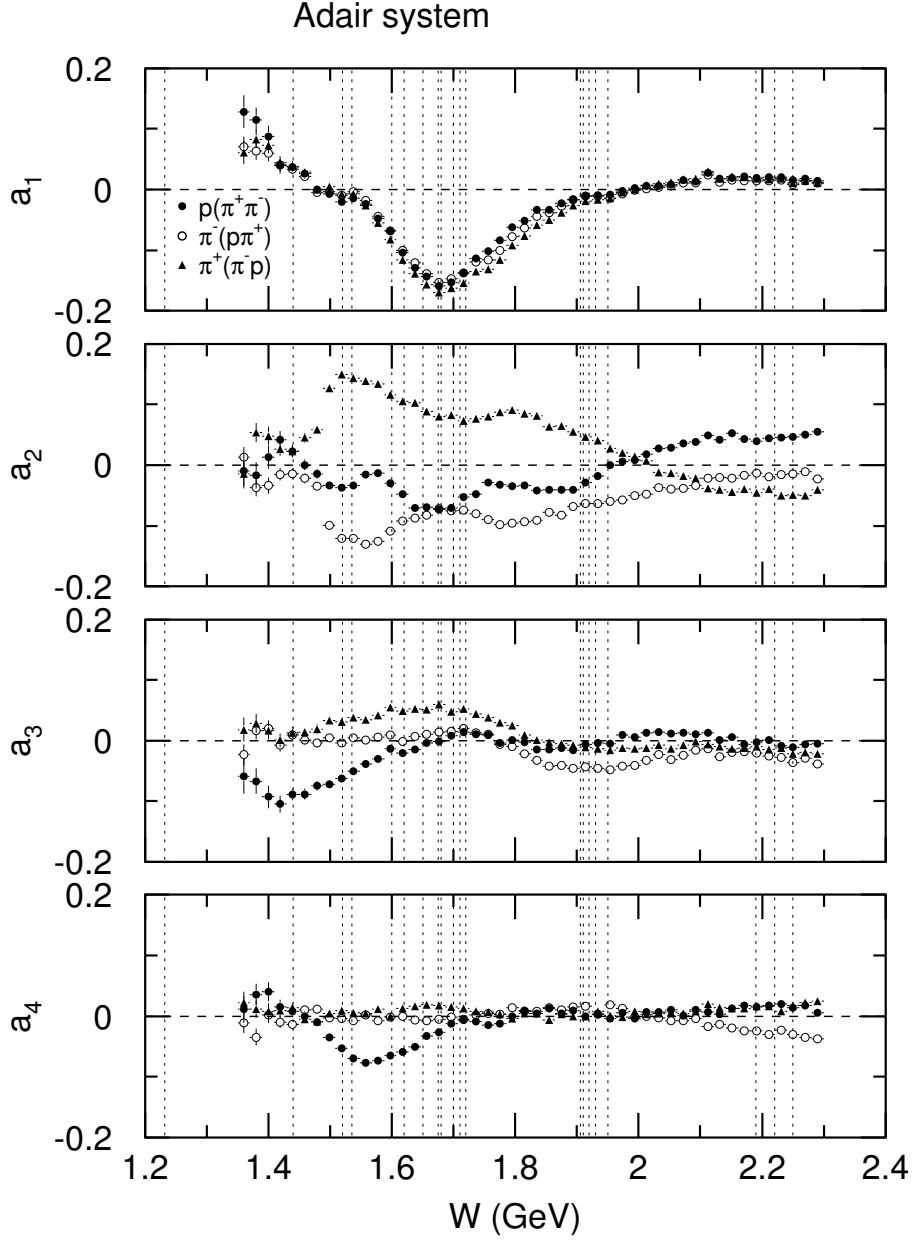
Figure 27: Fourier components of the $\gamma p \to p\pi^+\pi^-$ cross-section asymmetry in the Adair system as a function of the γp center-of-mass energy. The data for the various configurations were integrated over the full CLAS acceptance. The vertical lines indicate the masses of 3- and 4-star resonances [1].
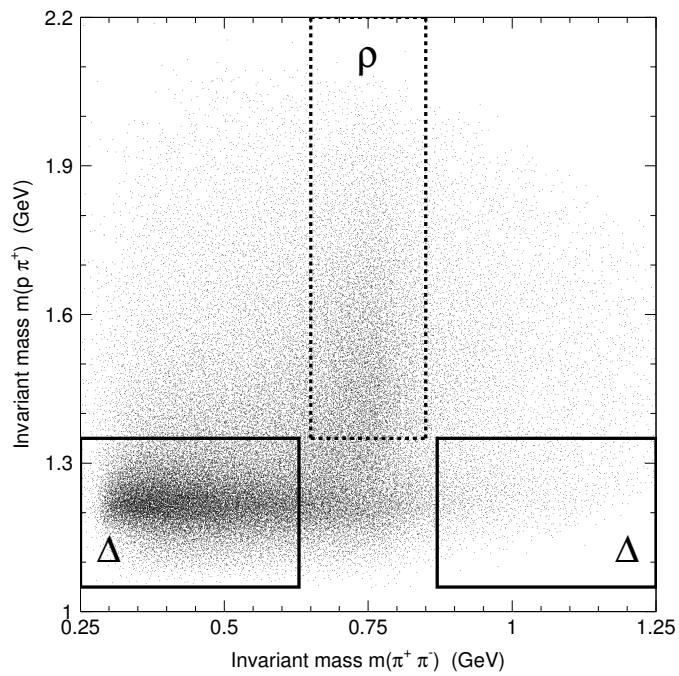
Figure 28: Event distribution as a function of the $\pi^+\pi^-$ and $p\pi^+$ invariant masses. The solid regions select events which mostly went through the $\Delta^{++}\pi^-$ channel, and the dashed region selects events dominated by the $N\rho$ channel.
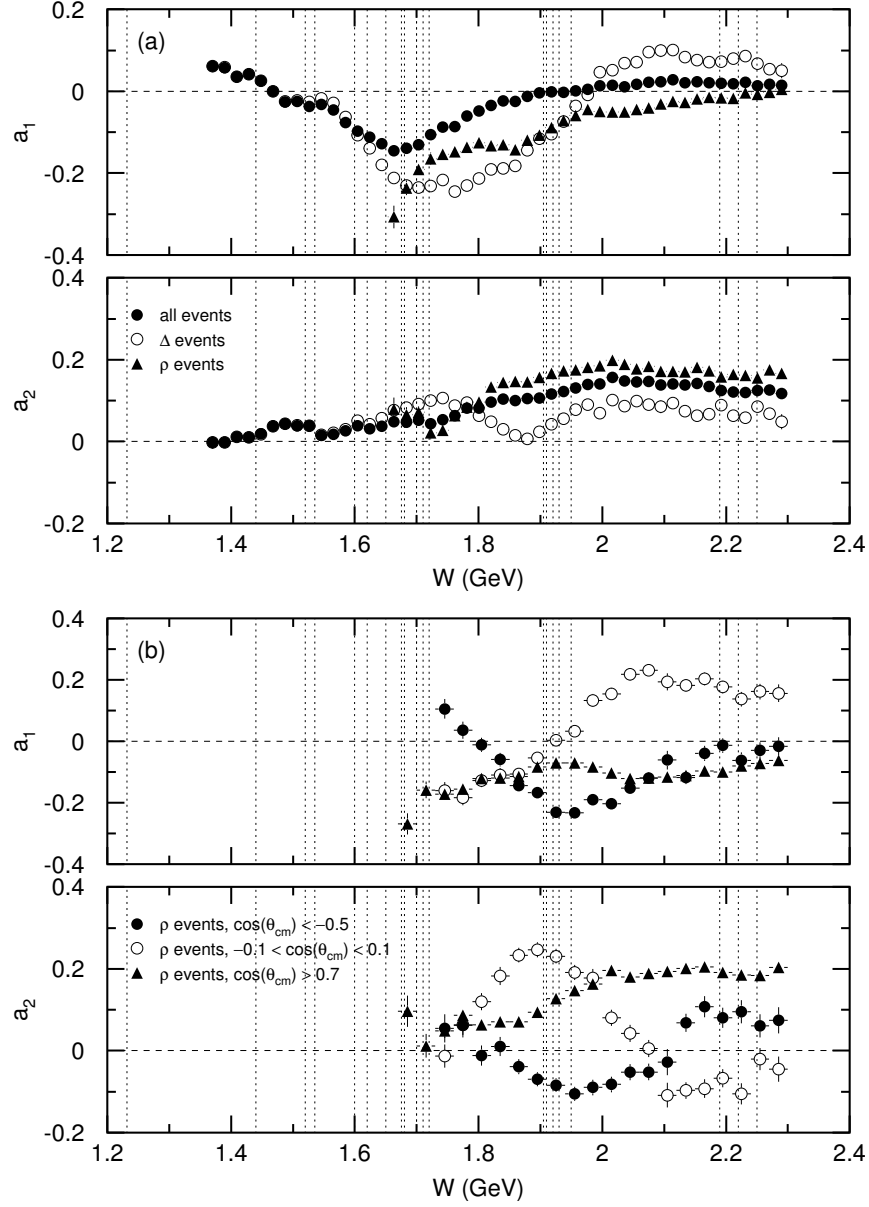
Figure 29: Fourier components of the $\gamma p \rightarrow p\pi^+\pi^-$ cross-section asymmetry as a function of the γp center-of-mass energy. The data in the $p[\pi^+, \pi^-]$ configuration were integrated over the full CLAS acceptance constrained by the following cuts: panel (a) all data (filled circles), Δ events (open circles) and ρ events (filled triangles) as denoted in Fig. 28; panel (b) ρ-event data with $\cos(\theta_{cm}) < -0.5$ (filled circles), $-0.1 < \cos(\theta_{cm}) < 0.1$ (open circles), and $\cos(\theta_{cm}) > 0.7$ (filled triangles). The vertical lines indicate the masses of 3- and 4-star resonances [1].

5.3   Comparison with calculations

Preliminary calculations for $\gamma p \to p\pi^+\pi^-$ cross-section asymmetries were done by Oed and Roberts [13] using a phenomenological Lagrangian approach. The formalism of the model is discussed in Ref. [14]. It is important to note that the calculations performed to date have been integrated over 4π, whereas the experimental data are integrated only over the CLAS acceptance. The results of the calculations are shown in Fig. 30 as solid curves. Calculations including the CLAS acceptance will be available soon. In general, a very good description of the data has been achieved.

Calculations have also been performed by Mokeev [15] in a phenomenological calculation using available information on N^* and Δ states. Parameters of this phenomenological code have been fitted to CLAS cross-section data for the real- and virtual-photon double-charged-pion production. The results are shown in Fig. 31; the model has not yet been adjusted to the polarization data and is preliminary. Using Eq. (23), the CLAS acceptance was taken into account in this calculation. There is clearly room for improvement in the model parameters.
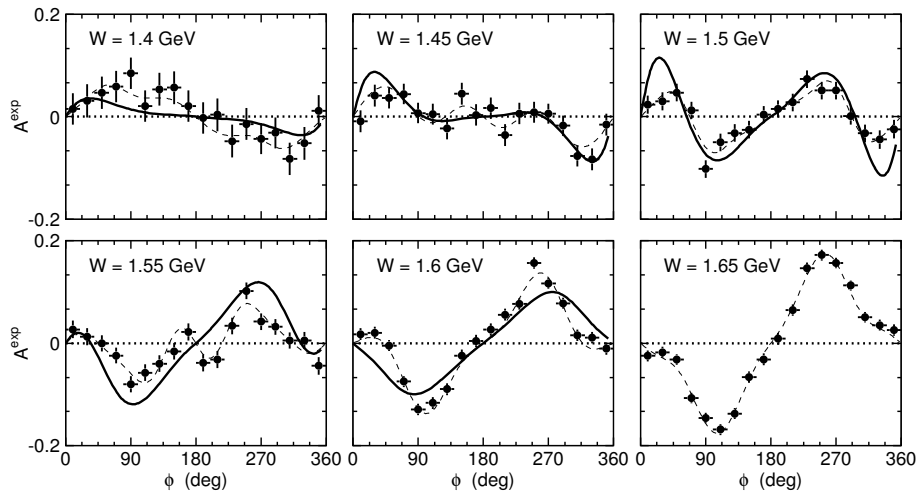

Figure 30: CLAS integrated azimuthal angular distribution of the cross-section asymmetry for six 25-MeV wide energy bins at $W = 1.40, 1.45, 1.50, 1.55, 1.60$, and 1.65 GeV for the configuration $p[\pi^+, \pi^-]$; panels (a) to (f). The solid curves are 4π-integrated calculations by Roberts [13, 14] (not for the highest energy). The dashed curves are fits of Eq. (25) up to order $n = 5$ to the data.

It is desirable to examine the sensitivity of the asymmetry to various theoretical model parameters. In fact, current studies have indicated a strong sensitivity of the helicity asymmetries to relative contributions of various isobaric channels and the interference among them. An example is shown in Fig. 32, where the $\gamma p \to p\pi^+\pi^-$ asymmetry data at $W = 1.84$ GeV for the configuration $\pi^-[p, \pi^+]$ are compared with various calculations by Mokeev [16]. These calcu-
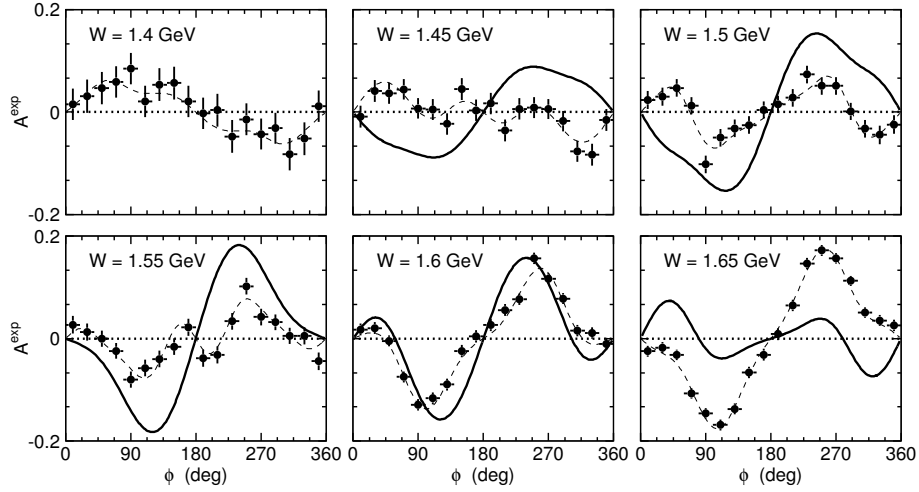
Figure 31: Same as Fig. 30, except for the solid curves which are calculations by Mokeev [15]. These calculations are event-weighted, according to Eq. (23), to account for the CLAS acceptance.

lations differ only in the amplitude and phase of the diffractive rho-production term. The helicity asymmetry shows strong sensitivity to this model parameter, whereas the differential cross section does not. This confirms the importance of polarization observables for differentiating between model predictions.
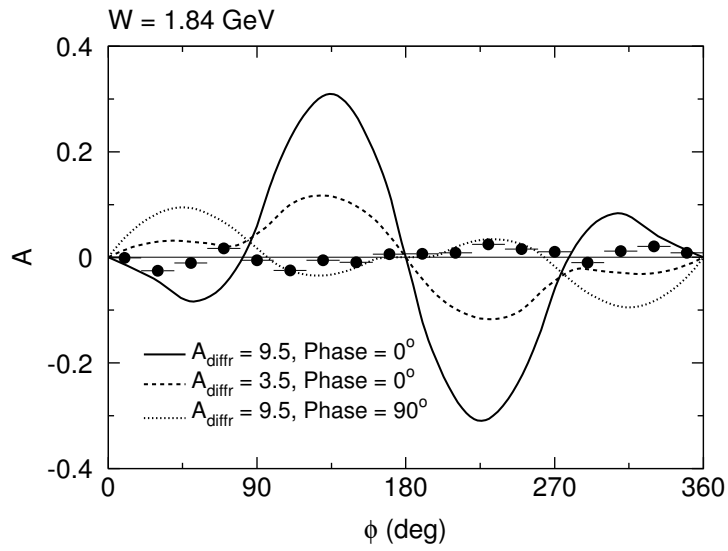
Figure 32: $\gamma p \to p\pi^+\pi^-$ angular distribution of the cross-section asymmetry at $W = 1.84$ GeV for the $\pi^-[p, \pi^+]$ configuration, along with the results of calculations by Mokeev with various choices for the diffractive rho-production amplitude [16].

6 Summary

In summary, angular distributions of large helicity-dependent cross-section asymmetries in the $\gamma p \to p\pi^+\pi^-$ reaction were observed for the first time, using the CLAS detector system. The analysis has revealed the rich structure inherent in these data. Preliminary comparisons with model calculations show that these asymmetries are sensitive to details of the reaction dynamics. These data will therefore prove to be an important tool in baryon spectroscopy.

References

[1] K. Hagiwara *et al.*, Phys. Rev. D **66**, 010001 (2002).

[2] M. Ripani *et al.*, Phys. Rev. Lett. **91**, 022002 (2003).

[3] S. Boffi, C. Guisti, F.D. Pacati, and M. Radici, *Electromagnetic Response of Atomic Nuclei* (Clarendon Press, Oxford, 1996).

[4] K. Schilling, P. Seyboth, and G. Wolf, Nucl. Phys. B **15**, 397 (1970).

[5] R.L. Thews, Phys. Rev. **175**, 1749 (1968).

[6] B. A. Mecking *et al.*, Nucl. Instrum. Methods **A503**, 513 (2003).

[7] D. I. Sober *et al.*, Nucl. Instrum. Methods **A440**, 263 (2000).

[8] J. McNabb, Ph.D. thesis, Carnegie Mellon University, 2002.

[9] L. Tudor, `http://clasweb.jlab.org/rungroups/g1c/g1c_gata.html`.

[10] E. Pasyuk, `momcor.F` (2003).

[11] H. Olsen and L. C. Maximon, Phys. Rev. **114**, 887 (1959)

[12] D. Protopopescu, F.W. Hersman, and M. Holtrop, "*Beam Polarization and Helicity Sign for the E2A Run Period,*" CLAS-ANALYSIS 2002-105.

[13] T. Oed and W. Roberts, private communication (2003).

[14] W. Roberts and A. Rakotovao, hep-ph/9708236.

[15] V. I. Mokeev *et al.*, Phys. At. Nucl. **66**, 1282 (2003); V. I. Mokeev *et al.*, Phys. At. Nucl. **64**, 1292 (2001), and references therein.

[16] V. I. Mokeev, private communication (2003).

A Uncertainty of the beam-charge asymmetry

The experimental asymmetry for the full data set is given by Eq. (18) and can be rewritten as

$$\bar{P}_\gamma A^{\text{exp}}(\Delta\tau) = \frac{\sum_i \frac{N_i^+}{\alpha_i^+} - \sum_i \frac{N_i^-}{\alpha_i^-}}{\sum_i \frac{N_i^+}{\alpha_i^+} + \sum_i \frac{N_i^-}{\alpha_i^-}} \ , \tag{26}$$

where the sums are running over all runs which belong to the full data set. Eq. (26) can to a very good approximation written as

$$\bar{P}_\gamma A^{\text{exp}}(\Delta\tau) \approx \frac{\sum_i N_i^+ - \sum_i N_i^-}{\sum_i N_i^+ + \sum_i N_i^-} - \underbrace{\frac{\sum_i a_{c,i}(N_i^+ + N_i^-)}{\sum_i (N_i^+ + N_i^-)}}_{\bar{a}_c} \ , \tag{27}$$

since the beam-charge asymmetry is much smaller than one, $|a_c| \ll 1$ and thus $(\alpha^\pm)^{-1} \approx 2(1 \mp a_c)$, and also $a_c(N^+ - N^-) \ll (N^+ + N^-)$. The second term in Eq. (27) is the event weighted mean value of the beam-charge asymmetries of each run. This term is equivalent to the mean value of a_c in Eq. (17) since the number of single-pion events ($N_\pi^\pm$) and the number of $\gamma p \to p\pi^+\pi^-$ events ($N^\pm$) are strictly proportional to each other for each run.

The distribution of $a_{c,i}$ is shown in Fig. 15. The mean value and width of the distribution are

$$\bar{a}_c \quad = \quad -0.0043, \tag{28}$$
$$\sigma(a_c) \quad = \quad 0.0026 \ . \tag{29}$$

It follows from Eq. (27) that a contribution to the uncertainty of the experimental asymmtry is given by the standard deviation of the sample mean $\sigma(\bar{a}_c)$, and not by the standard deviation of the sample $\sigma(a_c)$. Both are related to each other by the number of events in the sample, here the number of runs $n = 135$:

$$\sigma(\bar{a}_c) = \sigma(a_c)/\sqrt{n} = 0.00022 \tag{30}$$

A more complete error propagation taking into account the differrent weights in the runs with different statistics gives the final results as quoted in section 4.2.3:

$$\bar{a}_c = -0.00429 \pm 0.00013 \ . \tag{31}$$